

Myostatin regulates energy homeostasis through autocrine- and paracrine-mediated microenvironment communications

Hui Wang, ... , Tiemin Liu, Xingxing Kong

J Clin Invest. 2024. <https://doi.org/10.1172/JCI178303>.

Research In-Press Preview Endocrinology

Myostatin (MSTN) has long been recognized as a critical regulator of muscle mass. Recently, there has been an increasing interest in its role in metabolism. In our study, we specifically knocked out MSTN in brown adipose tissue (BAT) from mice (MSTN^{ΔUCP1}) and found that the mice gained more weight than controls when fed a high-fat diet, with progressive hepatosteatosis and impaired skeletal muscle activity. RNA-seq analysis indicated signatures of mitochondrial dysfunction and inflammation in the MSTN-ablation BAT. Further studies demonstrated that the Kruppel-like factor 4 (KLF4) was responsible for the metabolic phenotypes observed, while FGF21 contributed to the microenvironment communication between adipocytes and macrophages induced by the loss of MSTN. Moreover, the MSTN-SMAD2/3-p38 signaling pathway mediated the expression of KLF4 and FGF21 in adipocytes. In summary, our findings suggest that brown adipocytes-derived MSTN regulates BAT thermogenesis via autocrine and paracrine effects on adipocytes or macrophages, ultimately regulating systemic energy homeostasis.

Find the latest version:

<https://jci.me/178303/pdf>



Myostatin regulates energy homeostasis through autocrine-and paracrine-mediated microenvironment communications

Hui Wang ^{1,*}, Shanshan Guo ^{1,*}, Huanqing Gao ^{1,*}, Jiyang Ding ^{1,*}, Hongyun Li ^{2,*}, Xingyu Kong ¹, Shuang Zhang ¹, Muyang He ^{3,5}, Yonghao Feng ⁴, Wei Wu ⁷, Kexin Xu ¹, Yuxuan Chen ¹, Hanyin Zhang ⁵, Tiemin Liu ^{1,3,6}, Xingxing Kong ^{1,7,#}

1. State Key Laboratory of Genetic Engineering and School of Life Sciences, Shanghai Key Laboratory of Metabolic Remodeling and Health, Institute of Metabolism and Integrative Biology, Human Phenome Institute, Fudan University, Shanghai 200438, China

2. Department of Sports Medicine and Arthroscopy Surgery, Huashan Hospital, Fudan University, Shanghai, China.

3. Department of Endocrinology and Metabolism, Zhongshan Hospital, Fudan University, Shanghai 200032, China

4. Department of Endocrinology, Jinshan Hospital, Fudan University, Shanghai 201508, China

5. Shanghai Medical College, Fudan University, Shanghai 200433, China

6. School of Life Sciences, Inner Mongolia University, Hohhot, Inner Mongolia 010021, China

7. Department of Endocrinology and Metabolism, Huashan Hospital, Fudan University, Shanghai 200040, China

* These authors contributed equally.

Address correspondence to: Xingxing Kong, State Key Laboratory of Genetic Engineering and School of Life Sciences, Shanghai Key Laboratory of Metabolic Remodeling and Health, Institute of Metabolism and Integrative Biology, Human Phenome Institute, Fudan University, Shanghai 200438, China. Phone: 86.21.31246753; Email: kongxingxing@fudan.edu.cn (X.K.)

Abstract

Myostatin (MSTN) has long been recognized as a critical regulator of muscle mass. Recently, there has been an increasing interest in its role in metabolism. In our study, we specifically knocked out MSTN in brown adipose tissue (BAT) from mice (MSTN^{ΔUCP1}) and found that the mice gained more weight than controls when fed a high-fat diet, with progressive hepatosteatosis and impaired skeletal muscle activity. RNA-seq analysis indicated signatures of mitochondrial dysfunction and inflammation in the MSTN-ablation BAT. Further studies demonstrated that the Kruppel-like factor 4 (KLF4) was responsible for the metabolic phenotypes observed, while FGF21 contributed to the microenvironment communication between adipocytes and macrophages induced by the loss of MSTN. Moreover, the MSTN-SMAD2/3-p38 signaling pathway mediated the expression of KLF4 and FGF21 in adipocytes. In summary, our findings suggest that brown adipocytes-derived MSTN regulates BAT thermogenesis via autocrine and paracrine effects on adipocytes or macrophages, ultimately regulating systemic energy homeostasis.

Introduction

Brown adipose tissue (BAT) plays a crucial role in whole-body energy balance and fuel metabolism, mediating non-shivering thermogenesis in mammals exposed to sub-thermoneutral temperatures (1). The abundance of mitochondria and expression of UCP1 in thermogenic adipocytes equip brown fat with a unique thermogenic capacity (2). Furthermore, BAT is now recognized as a dynamic endocrine organ, secreting adipokines, gaseous messengers, and microvesicles that can target distant tissues such as white adipose tissue, liver, pancreas, heart, and bone (3, 4). Experimental studies involving BAT transplantation and activation have demonstrated notable improvements in metabolism and cardiac protection through the release of endocrine factors such as insulin-like growth factor I, interleukin-6, and fibroblast growth factors (5). In a previous study, we demonstrated that the knockout of interferon regulatory factor 4 in brown fat cells could reduce the secretion of myostatin, impairing the exercise capacity of mice (6). However, the role of myostatin in brown fat cells remains unclear.

Myostatin (MSTN; also known as growth differentiation factor 8, belongs to the transforming growth factor β (TGF β) superfamily and serves as a critical regulator of skeletal muscle mass (7). Inhibitors targeting the MSTN signaling pathway have been developed for the treatment of sarcopenia and muscular dystrophy (8). However, the response to MSTN inhibitors in terms of functional improvements has been inconsistent. While increased muscle mass has been observed in most clinical trials, this often does not translate into clinically meaningful enhancements in strength (9, 10). However, targeting the MSTN signaling pathway consistently reduces fat mass (11-13). These observations align with findings from mouse studies, where MSTN global knockout mice exhibited increased muscle mass, reduced fat deposition, improved insulin sensitivity, enhanced fatty acid oxidation, and resistance to obesity (14, 15). Subsequent studies in mice treated with MSTN inhibitors have further elucidated the role of MSTN in metabolic regulation (16, 17). Notably, clinical observations have increasingly associated variations in myostatin expression with metabolic conditions. For instance, elevated myostatin levels have been observed in individuals with obesity and insulin resistance, implicating it in the pathophysiology of metabolic syndrome (18). Conversely, reduced myostatin activity is linked to increased muscle mass and improved metabolic profiles, suggesting a protective role against metabolic dysfunction (8). Conversely, reduced myostatin activity is linked to increased muscle mass and improved metabolic profiles, suggesting a protective role against metabolic dysfunction (8). Additionally, MSTN deletion has been found to prevent age-related increases in adipose tissue mass and partially improves obesity diabetes in mice (19). Furthermore, specific overexpression of MSTN in adipose tissue has been demonstrated to increase metabolic rate and resistance to diet-induced obesity (20). The dual role of myostatin in muscle and adipose tissue underscores its potential as a therapeutic target. Clinical studies have explored

1 myostatin inhibitors in muscle-wasting diseases, noting improvements in
2 muscle mass and preliminary indications of metabolic benefits. These
3 observations raise compelling questions about the broader implications of
4 myostatin modulation in metabolic health, particularly through its effects on
5 adipose tissues.

6 Kruppel-like factor (KLF) 4 is a member of a large family of zinc-finger
7 proteins, critical for various development processes, including differentiation,
8 proliferation, and inflammation. KLF4 serves as an essential early regulator of
9 adipogenesis, by regulating C/EBP β (21). Moreover, cells deficient in KLF4
10 exhibit mitochondrial dysfunction and impaired mitophagy (22). Specifically, in
11 KLF4-null cells, there is a reduction in the expression of the mitophagy-
12 associated protein Bnip3 and antioxidant protein GST α 4 (22). Despite
13 substantial contextual evidence of KLF4's role in development, the specific
14 molecular mechanisms in metabolism, especially in brown adipose tissue, are
15 unclear.

16 Fibroblast growth factor 21 (FGF21), a member of the endocrine FGF
17 subfamily, has pleiotropic effects on energy homeostasis. Emerging clinical
18 evidence demonstrates that elevated circulating FGF21 can be used as a
19 biomarker of metabolic diseases such as metabolic dysfunction-associated
20 steatohepatitis (MASH) and type 2 diabetes (23, 24). Notably, several FGF21
21 analogs and mimetics have progressed to early phases of clinical trials in
22 patients with obesity, type 2 diabetes mellitus and MASH (25). Global deletion
23 of FGF21 in mice leads to impairments in cold-induced browning of inguinal
24 white adipose tissue (iWAT), while administration of recombinant FGF21
25 increases browning and total energy expenditure in mice (26). Huang et al
26 reported that adipocytes-derived FGF21 exerts autocrine effects, inducing
27 CCL11 production in adipocytes to promote recruitment of eosinophils, thereby
28 stimulating M2 macrophages activity (27). However, it is currently unclear what
29 regulates FGF21 in adipocytes.

30 The present study found that mice with brown adipocyte-specific deletion
31 of MSTN exhibited diet-induced insulin resistance, glucose intolerance, and
32 hepatosteatosis, contrary to the phenotypes of MSTN global knockout mice.
33 Furthermore, BAT-specific knockout of MSTN led a significant reduction in
34 browning and adaptive thermogenesis. Mechanistic studies revealed that
35 MSTN regulates the expression of KLF4 and FGF21 via the SMAD2/3 and p38
36 signaling pathways in adipocytes. The decreased levels of KLF4 and FGF21
37 contribute to MSTN deficiency-induced mitochondrial dysfunction and
38 inflammation, respectively. These findings provide critical insights into the
39 function of myostatin in BAT and its potential as a modulator of metabolic health,
40 paving the way for novel interventions targeting BAT function to ameliorate
41 obesity and metabolic diseases.

42 43 **Results**

44 **Mice with BAT-specific Myostatin knockout are prone to diet-induced**

obesity

Previous studies have suggested that BAT-derived MSTN may play a role in energy metabolism (6, 28). To further investigate the role of MSTN in regulating BAT homeostasis, we examined the expression of MSTN in response to varying nutrient states. Our findings revealed a reduction in MSTN expression in the diet-induced obesity (DIO) mouse model (Fig. 1A, B).

Subsequently, we generated Myostatin flox/flox (Flox) mice and crossed them with CAG-cre (MSTN^{ΔCAG}) to mimic the effects observed in Myostatin-global knockout mice (7). Notably, the MSTN^{ΔCAG} mice were noticeably more muscular than the control mice when fed a chow diet (Extended Data Fig. 1A, B). Additionally, the heterozygous MSTN^{ΔCAG} mice showed resistance to DIO, with reduced fat mass but increased lean mass compared to the controls (Extended Data Fig. 1C, D). Adipocyte size was also smaller in adipose tissue from heterozygous MSTN^{ΔCAG} mice on a high-fat diet (HFD) (Extended Data Fig. 1E).

We then crossed the Flox mice with UCP1-Cre mice to study the thermogenic function of Myostatin. The protein and mRNA levels of MSTN were markedly decreased in BAT but remained normal in other tissues (Fig. 1C, D). The protein levels of MSTN in plasma were not altered in the MSTN^{ΔUCP1} mice compared to the Flox mice (Extended Data Fig. 2A), indicating Myostatin deletion in BAT does not affect the circulating levels of MSTN. Compared to the Flox group, BAT-specific Myostatin knockout male mice (MSTN^{ΔUCP1} hereafter) showed no defective developmental and metabolic phenotypes in body weight and body composition when fed a normal chow (NC) diet (Extended Data Fig. 2B-I). Surprisingly, unlike the MSTN^{ΔCAG} mice, the MSTN^{ΔUCP1} mice exhibited a more pronounced increase in body weight and adiposity, without marked changes in their lean mass when fed an HFD (Fig. 1 E-H). The increased body weight and adiposity were also observed in female mice (Extended Data Fig. 2J, K). To address developmental concerns, we crossed Rosa26^{CAG-LSL-Cas9-tdTomato} mice with the UCP1-Cre transgenic mice and obtained the UCP1-Cre; Cas9 mice. We in situ injected AAV-sgMstn into BAT to specifically knockout Myostatin in BAT of the UCP1-Cre mice. The protein levels of MSTN were markedly decreased in BAT (Extended Data Fig. 2L), while the phenotypes of AAV8-sgMstn mice were consistent with those of BKO mice (Extended Data Fig. 2M, N). Furthermore, the MSTN^{ΔUCP1} mice displayed a more deteriorative adipose tissue phenotype characterized by larger adipocytes (Fig. 1I), opposite to those observed in Myostatin-global knockout mice (29). Additionally, the MSTN^{ΔUCP1} mice displayed insulin resistance (Fig. 1J-M). To determine whether brown adipocyte Myostatin deficiency affects energy balance, the mice were subjected to metabolic cages. The oxygen consumption (VO₂), carbon dioxide production (VCO₂), respiratory exchange rate (RER), and energy expenditure were lower in the MSTN^{ΔUCP1} mice compared to control littermates (Fig. 1N-Q). To confirm the role of Myostatin in adaptive thermogenesis, the mice were subjected to cold stress. As expected, the MSTN^{ΔUCP1} mice were

1 cold intolerant (Fig. 1R). In summary, loss of Myostatin in brown adipocytes
2 resulted in impaired energy expenditure, different from the phenotypes of
3 observed in the Myostatin-global knockout mice.

4 **MSTN^{ΔUCP1} mice exhibit progressive fatty liver**

5 To evaluate whether BAT MSTN affects systemic metabolism, we
6 performed targeted metabolomics, encompassing 600 metabolites. The
7 principal component analysis (PCA) revealed a clear distinction between the
8 BKO and Flox groups (Fig. 2A). Elevated levels of triglycerides (TG) and
9 ceramides were observed in plasma from the MSTN^{ΔUCP1} mice (Fig. 2B). In
10 addition to TG, cholesterol (TC) were also increased in the Myostatin-knockout
11 mice (Fig. 2C). Given that hepatic steatosis is closely associated with obesity
12 and insulin resistance, we next assessed the effects of MSTN deletion on
13 hepatic lipid deposition under HFD condition. Elevated levels of TG and TC
14 were observed in the liver of the MSTN^{ΔUCP1} mice (Fig. 2D). The liver mass of
15 the MSTN^{ΔUCP1} mice was heavier than that of control mice after HFD feeding
16 (Fig. 2E). The MSTN^{ΔUCP1} mice showed more lipid accumulation in the liver than
17 controls (Fig. 2F). The mRNA levels of fatty acid synthesis genes, such as fatty
18 acid synthase (Fas) and sterol regulatory element-binding protein-1c (Srebp-
19 1c) were markedly increased in the liver from the BKO mice compared to control
20 mice (Fig. 2G). Conversely, the expression of lipolysis genes, including Pnpla2
21 and Lipe, was decreased compared to controls (Fig. 2G). Similar impairments
22 in lipid metabolism were observed in AAV8-sgMstn mice (Fig. 2H). Thus, BAT-
23 specific MSTN deficiency aggravates hepatic steatosis.

24 **Ablation of Myostatin in BAT impairs skeletal muscle function**

25 Despite the comparable lean mass of MSTN^{ΔUCP1} mice with controls, unlike
26 the extremely muscular phenotype observed in MSTN global mutant animals
27 (7), skeletal muscle function was impaired. Grip strength and exercise capacity
28 were both lower in the MSTN^{ΔUCP1} mice compared to the Flox mice (Fig. 3A, B).
29 Additionally, the latency of muscle contraction was prolonged in the MSTN^{ΔUCP1}
30 mice (Fig. 3C). Consistent with, the oxygen consumption rate (OCR) was
31 decreased in muscle from the MSTN^{ΔUCP1} mice (Fig. 3D). Different muscle fiber
32 types were reported to contribute to muscle strength (30). Interestingly, in the
33 MSTN^{ΔUCP1} mice, exhibited a decrease in the proportion of type IIa muscle
34 fibers, whereas there was no significant difference in cross-section area of the
35 fibers (Fig. 3E-G). Skeletal muscle injuries are common occurrences in daily
36 life and exercise, and the capacity for regeneration is critical for muscle repair
37 and functional maintenance. We injected cardiotoxin (CTX), which can induce
38 a transient and reproducible acute injury without affecting the vasculature or
39 nerves (31), into the tibialis anterior (TA) muscle. The MSTN^{ΔUCP1} mice
40 exhibited delayed muscle regeneration compared to the control mice (Fig. 3H).

41 Lipid accumulation in skeletal muscles is implicated in insulin resistance
42 and type 2 diabetes (32). Therefore, we measured the TG levels in muscle,
43 revealing an increase in TG levels in muscles from the MSTN^{ΔUCP1} mice (Fig.
44 3I). The MSTN^{ΔUCP1} mice exhibited greater lipid accumulation in the

gastrocnemius (GAS) compared to controls (Fig. 3J). Electron microscopy images showed an elevated number of lipid droplets in muscle from $MSTN^{\Delta UCP1}$ mice compared to controls (Fig. 3K). RNA-seq analysis revealed 227 downregulated genes and 96 upregulated genes in muscle from the $MSTN^{\Delta UCP1}$ mice compared to Flox mice (Fig. 3L). Pathway analysis suggested attenuation of lipid catabolism (Fig. 3M, N). Furthermore, quantitative polymerase chain reaction (QPCR) data revealed that genes of fatty acid oxidation were decreased in muscle from the $MSTN^{\Delta UCP1}$ mice (Fig. 3O). Impaired lipid metabolism in GAS was also observed in the AAV8-sgMstn mice (Fig 3P). Collectively, these findings demonstrated impaired lipid metabolism in muscle obtained from $MSTN^{\Delta UCP1}$ mice.

Loss of Myostatin attenuates mitochondrial biogenesis and mitophagy

Myostatin has been reported to influence adipogenesis in vitro (20). To further explore this, we overexpressed Myostatin in stromal vascular fractions (SVFs) and then induced their differentiation into adipocytes, where we observed inhibition of adipogenesis (Extended Data Fig. 3A). However, we did not observe alterations in adipogenic gene expression in BAT from the $MSTN^{\Delta UCP1}$ mice (Extended Data Fig. 3B). Nonetheless, we noted a decrease in thermogenic gene expression in Myostatin deficient BAT (Fig. 4A, Extended Data Fig. 3C). Additionally, protein levels of PGC1 α , a key gene involved in mitochondrial biogenesis, and uncoupling protein 1 (UCP1) were decreased as well (Fig. 4B, C). These two proteins were down-regulated in primary brown adipocytes with knockdown of Myostatin (Extended Data Fig. 3D).

Given BAT is rich in mitochondria, we analyzed mitochondrial dynamics. Electron microscopy revealed a loss of Myostatin decrease in mitochondrial number in $MSTN$ -deficient BAT compared to controls (Fig. 4D, E). Additionally, some proteins associated with the mitochondrial complex were decreased, including SDHB and NDUFB8 (Fig. 4F). Mitophagy, necessary for maintaining BAT mitochondrial integrity and optimal BAT thermogenesis, was also impaired (33). Proteins involved in mitophagy (PINK1 and LC3) were down-regulated, while p62 was up-regulated in Myostatin-deficient BAT (Fig. 4G) and primary brown adipocytes (Extended Data Fig. 3E). This was further confirmed by electron microscopy (Fig. 4H). In line with these findings, mitochondrial function was decreased, as evidence by reduced oxygen consumption (Fig. 4I).

Myostatin global knockout mice has previously been shown to induce the browning of white adipose tissue in mice (34). However, this was not the case in $MSTN^{\Delta UCP1}$ mice. The $MSTN^{\Delta UCP1}$ mice had a lower core body temperature than control mice after 7 days of cold exposure (Fig. 4J). Thermography assessment indicated a reduction in surface temperature specifically at the interscapular region in the $MSTN^{\Delta UCP1}$ mice (Fig. 4K). Additionally, there were decreased induction of UCP1-expressing beige adipocytes and downregulation of cold-induced UCP1 expression in inguinal white adipose tissue (iWAT) from the $MSTN^{\Delta UCP1}$ mice (Fig. 4L-N). Furthermore, the mitophagy protein levels were decreased in iWAT when the $MSTN^{\Delta UCP1}$ mice were exposed to cold

temperatures (Fig. 4O). These findings suggested that Myostatin plays a critical role in adaptive thermogenesis and the browning of iWAT.

Ablation of Myostatin in BAT shows signatures of mitochondrial dysfunction and inflammation

In our subsequent investigation, we delved into elucidating the molecular mechanism of Myostatin in BAT. RNA-seq was performed, and the PCA analysis revealed difference between the BKO and Flox groups (Fig. 5A). We found that 414 differential expressed genes (DEGs) were up-regulated, while 202 DEGs were down-regulated (Fig. 5B). The Kyoto Encyclopedia of Genes and Genomes (KEGG) pathway analysis indicated that oxidative phosphorylation was inhibited (Fig. 5C), which was consistent with the observed alterations in mitochondrial function (Fig. 4). However, inflammation was enhanced in Myostatin-KO BAT (Fig. 5D). Furthermore, the M1-like macrophage marker genes, which are pro-inflammatory, were increased, while M2-like genes, which are anti-inflammatory, were decreased (Fig. 5E, Extended Data Fig. 4A). The F4/80 staining indicated that there were more crown-like structures in Myostatin-KO BAT compared to the control (Fig. 5F). Nonetheless, contrasting observations were noted in BAT from MSTN^{ΔCAG} mice (Extended Data Fig. 4B). To explore the potential paracrine effects of MSTN-KO adipocytes on BAT-resident macrophages, we conducted co-culture experiments using transwell systems. The gene expression panels obtained from these experiments were similar to those observed in vivo (Fig. 5G). Conversely, no differences in inflammatory genes were observed between co-cultured with Myostatin-KO and control mature adipocytes (Extended Data Fig. 4C, D), suggesting the involvement of additional cell types in the regulatory interplay between brown adipocytes and macrophages.

The literature underscores the multifaceted role of KLF4, an essential transcriptional factor in development, in regulating both mitochondrial activity and inflammation (35-38). Therefore, KLF4 expression was measured. The mRNA and protein levels of KLF4 were decreased in Myostatin-KO BAT (Fig. 5H, I). Similar observations were made following the knockdown of Myostatin in primary adipocytes (Extended Data Fig. 4E). Furthermore, Chip-qPCR results revealed that KLF4 binds to the Pink1 promoter at -461---470 and -552--561 (Extended Data Fig. 4F). Next, we investigated the mechanism underlying the regulation of KLF4 in adipocytes. Notable, Myostatin can activate both SMAD or non-SMAD pathways to execute its functions (39) (Fig. 5J). The phosphorylation of SMAD2/3 was decreased when upon KO of Myostatin (Fig. 5K, Extended Data Fig. 4G). Among the non-SMAD targeted signaling pathways, only the phosphorylation of p38 was decreased, no changes in either ERK or JNK (Fig. 5K). Treatment with inhibitors targeting SMAD2/3 (TP0427736 HCl) or p38 (SB 202190) resulted in a notable decrease in the protein levels of KLF4 (Fig. 5L, M). Conversely, administration of a p38 agonist (dehydrocorydaline) effectively restored the protein levels of KLF4 in the MSTN-KO BAT (Fig. 5N). Additionally, KLF4 expression exhibited an increase in

adipocytes treated with recombinant MSTN (rMSTN); however, this effect was counteracted upon treatment with TP0427736 HCl and SB 202190 (Fig. 5O). These findings indicate that the p38 pathway regulates KLF4 expression (40) and that MSTN regulates KLF4 via SMAD2/3 and p38 pathways.

KLF4 is required for the metabolic phenotypes induced by Myostatin ablation

To verify whether KLF4 is pivotal for the metabolic phenotypes induced by Myostatin ablation, we overexpressed KLF4 in BAT via direct injection of AAV-KLF4 (Fig. 6A). Notably, the expression of KLF4 in iWAT, GAS, and liver remained unchanged (Extended Data Fig. 5A-C). Four weeks post injection, the body weight and body mass were decreased and returned to normal in the AAV-KLF4-treated MSTN^{ΔUCP1} mice (Fig. 6B, C). Additionally, the adipocyte size in both BAT and iWAT was notably smaller in the AAV-KLF4-treated MSTN^{ΔUCP1} mice compared to the AAV-GFP-treated MSTN^{ΔUCP1} mice (Fig. 6D). Moreover, glucose tolerance test (GTT) and insulin tolerance test (ITT) were rescued following AAV-KLF4 injection (Fig. 6E, F). Similarly, energy expenditure was rescued (Fig. 6G-I, Extended Data Fig. 5D-G). Cold tolerance tests further demonstrated that overexpression of KLF4 ameliorated the intolerance (Fig. 6J). The levels of serum TG and TC were lower in the AAV-KLF4-treated MSTN^{ΔUCP1} mice compared to the AAV-GFP-treated MSTN^{ΔUCP1} mice (Fig. 6K, L). Additionally, the expression of genes related to fatty acid metabolism was back to normal in the liver and muscle (Fig. 6M, N).

The expression of thermogenic genes, such as PGC1 α and UCP1, were decreased in Myostatin-KO BAT; however, their levels were notably restored upon overexpression of KLF4 (Fig. 6O, P). UCP1 staining of BAT further revealed an increase in UCP1⁺ cells in response to KLF4 overexpression (Fig. 6Q). Furthermore, overexpression of KLF4 effectively mitigated the mitochondrial dysfunction induced by the loss of Myostatin, as evidenced by the restoration of proteins associated with mitochondrial complex and mitophagy (Fig. 6R, S). In primary brown adipocytes, the knockdown of Myostatin decreased the protein levels of PGC1 α and UCP1. However, supplementation with KLF4 successfully restored these proteins to normal levels (Extended Data Fig. 5H). Although most of the Myostatin KO-induced phenotypes were counteracted by KLF4 overexpression, it is noteworthy that the expression of inflammatory genes remained unaltered (Fig. 6T).

FGF21 is responsible for the inflammatory phenotypes induced by Myostatin ablation

FGF21 was studied to mediate the crosstalk between adipocytes and macrophages (27). We thus investigated whether FGF21 accounts for the inflammation induced by Myostatin ablation. The expression of FGF21 was decreased in Myostatin-KO BAT (Fig. 7A, B), and the fractionation revealed that the decrease only occurred in mature adipocytes but not in stromal vascular fractions (SVFs) (Fig. 7C). Knockdown of Myostatin in primary brown adipocytes also inhibited the expression of FGF21 (Fig. 7D). p38 has been

1 reported to mediate FGF21 release in mice and adipocytes (41). Adipocytes
2 treated with a p38 inhibitor exhibited decreased FGF21 expression (Fig. 7E).
3 However, treatment with a p38 agonist restored the protein levels of FGF21 in
4 Myostatin-KO BAT (Fig. 7F). Although several studies have reported that
5 FGF21 exerts its functions via the phosphorylation levels of SMAD2/3 (42-44),
6 inhibition of SMAD2/3 decreased the expression of FGF21 (Fig. 7G).
7 Additionally, rMSTN upregulated the expression levels of FGF21; however, the
8 expression levels were restored to normal upon treatment with TP0427736 HCl
9 and SB 202190 (Fig. 7H).

10 To explore the role FGF21 in Myostatin-KO-induced inflammation, we
11 introduced recombinant FGF21 (rFGF21) into a co-culture system. The addition
12 of rFGF21 successfully reversed the expression of inflammatory genes induced
13 by BAT from MSTN^{ΔUCP1} mice (Fig. 7I). FGF21 probably inhibited macrophage-
14 mediated inflammation by suppressing the NF-κB signaling pathway, as
15 evidenced by the downregulation of Relα, Relβ, c-Rel in co-cultured
16 macrophages treated with rFGF21 (Fig. 7J). Consistent with Xu's study (27), it
17 is suggested that adipocytes derived-FGF21 may indirectly modulate
18 macrophage mediated inflammation, as rFGF21 had no effects on
19 macrophages when co-cultured with mature adipocytes (Extended Data Fig.
20 6A). Additionally, a single injection of rFGF21 directly into BAT resulted in
21 decreased expression of inflammatory genes (Extended Data Fig. 6B).
22 Importantly, this treatment did not alter serum TG or TC levels (Extended Data
23 Fig. 6C, D). To further verify whether FGF21 is required for the Myostatin-KO-
24 induced inflammatory phenotype, we overexpressed FGF21 in BAT using AAV-
25 FGF21. Interestingly, inflammation resolved in BAT of BKO mice
26 overexpressing FGF21. However, metabolic phenotypes such as mitochondrial
27 function, liver TG, and lipid metabolism in the liver and gastrocnemius muscle
28 were not restored to normal levels (Fig. 7K, Extended Data Fig. 6E-K).

30 Discussion

31 MSTN is well-known as a key inhibitor of skeletal muscle growth. Although
32 several studies have addressed the endocrine effect of MSTN on adipose
33 tissue, the results have been controversial. The present study provides a series
34 of evidence indicating that brown adipocyte-derived MSTN serves as a key
35 triggering factor for energy homeostasis via its autocrine and paracrine actions
36 within the metabolic niche of BAT (Fig. 7I). In Myostatin-KO adipocytes, the
37 expression of KLF4 and FGF21 was decreased due to inhibition of the
38 SMAD2/3 and p38 signaling pathways. Treatment with KLF4 ameliorated all the
39 metabolic phenotypes induced by Myostatin ablation, except inflammation.
40 FGF21 was proven to contribute to Myostatin-KO-induced inflammation. These
41 findings demonstrate an important role of brown adipocyte-derived MSTN in
42 metabolism, different from the phenotypes in the global KO mice, suggesting
43 MSTN has cell/ tissue-specific effects.

44 Accumulating in vitro and in vivo data from diverse laboratories in recent

years supports the notion that inhibition of MSTN, either through pharmacological modulation or genetic inactivation, increases brown adipose characteristics, enhances energy expenditure, and provides metabolic benefits (19). However, specific inhibition of MSTN signaling, achieved through overexpression of a dominant negative activin IIB receptor in adipocytes or skeletal muscle, reveals contrasting findings. While inhibition in muscle leads to reduced fat mass and improved insulin sensitivity, the direct impact on adipose tissue remains less pronounced, suggesting that changes in glucose metabolism and adiposity in MSTN-null mice may primarily stem from alterations in skeletal muscle function rather than direct effects on adipose tissue (45). However, Feldman et al. reported that ectopic production of myostatin, specifically in adipose tissue, induces adipose wasting (20). Consistent with this, our MSTN^{ΔUCP1} mice exhibited diet-induced obesity, with insulin resistance, impaired energy expenditure, cold intolerance, and hepatosteatosis. These data indicate that the phenotypes between MSTN^{ΔUCP1} and Myostatin-null mice are different. Several interpretations can be drawn. Firstly, it's plausible that brown adipocytes-derived Myostatin regulates mitochondrial function via autocrine or intracellular effects, by enhancing KLF4-mediated mitochondrial turnover. Secondly, Myostatin may regulate the expression of FGF21 in adipocytes, with FGF21 acting as a secretion factor to modulate immune cells in BAT, thereby serving as a physiological integrator of metabolism and immunity. Thirdly, differences in adipocyte size between MSTN^{ΔUCP1} and Myostatin-null mice—larger in the former and smaller in the latter—suggest distinct endocrine and paracrine roles of Myostatin in adipocyte precursors. Lastly, variations in the inflammatory state of BAT between MSTN^{ΔUCP1} (pro-inflammatory) and global knockout mice (anti-inflammatory) may elicit feedback responses in adipocytes and other niche cells, potentially mediated by Myostatin's role in immune cells, particularly macrophages.

Several studies have demonstrated that mutations in the Myostatin gene increase skeletal muscle mass in mice, cattle, sheep, dogs, and human (46). However, the MSTN^{ΔUCP1} mice in this study exhibited identical lean mass with impaired exercise performances. Given that BAT thermogenesis primarily relies on fatty acids hydrolyzed from intracellular TG (47), any impairment in BAT may result in increased TG levels. Notably, serum and muscle TG levels were found to be increased in the MSTN^{ΔUCP1} mice. Furthermore, the RNA-seq data indicated disordered lipid metabolism pathways in the MSTN^{ΔUCP1} mice, in contrast to the global KO mice. Additionally, the plasma MSTN levels remained unchanged in the MSTN^{ΔUCP1} mice compared to the Flox mice. These data indicate that brown adipocyte-derived Myostatin impairs systemic lipid metabolism.

ActRIIB serves as the type II receptor for MSTN, while ActRI and TβRI act as the type I receptors (48). MSTN signaling pathways include SMAD-mediated and non-SMAD (such as p38 MAPK, JNK, ERK) pathways (39). Among these, the p38 pathway has emerged as a key regulator of BAT

activation. While JNK activation is increased in adipose tissues of obese mice (49, 50), p38 activity is markedly decreased in the adipose tissue of mice with diet-induced or genetically induced (ob/ob) obesity (51). In line with this, the phosphorylation of p38 was found to be decreased in MSTN-null BAT. Our findings further demonstrate that Smad2/3 or p38 inhibitors can mimic the effects induced by MSTN knockdown in brown adipocytes. Additionally, previous studies have indicated that the p38 signaling pathway can regulate the expression of Klf4 and Fgf21 (41, 52). We herein addressed a pathway for Myostatin intracellular signals.

In summary, our study uncovered a novel physiological role of brown adipocyte-derived Myostatin-KLF4/FGF21 axis in regulating metabolic niche in BAT, thereby regulating systemic energy homeostasis. Although both animal and clinical studies have demonstrated promising effects of MSTN antibody in reducing body weight and increasing muscle mass (8), a better understanding of Myostatin in adipose tissue holds potential for novel and promising clinical applications in controlling body and fat weight, as well as animal production.

Methods

Sex as a biological variable

Male and female mice were used in this study.

Animals Mice were maintained under a 12-hours light/12-hours dark cycle at constant temperature (23°C) and humidity (50–60%) with free access to food and water. MSTN^{flox/flox} mice were generated using CRISPR/Cas9 technology. According to the conserved region and structure of MSTN gene, exon2-exon3 of MSTN (ENSMUSG00000026100) was set as the knockout region.

Animal experiment design 1# To confirm the role of MSTN in adipose tissue. We crossed Myostatin^{flox/flox} (Flox) mice with CAG-cre (MSTN^{ΔCAG}) to mimic the effects of Myostatin global knockout mice. The male WT and MSTN^{+/-} mice were treated with 60% high-fat diet (PD6001, Changzhou SYSE Bio-Tec. Co., Ltd.) to generate obese model.

Animal experiment design 2# To further investigate whether Myostatin participates in regulating BAT homeostasis, we generated brown adipose tissue specific MSTN knockout mice. To delete Myostatin expression in BAT, we crossed the MSTN^{Flox/Flox} mice with the UCP1-Cre transgenic mice and obtained the UCP1-Cre; MSTN^{Flox/Flox} (referred to as BKO, MSTN^{ΔUCP1}) mice. The Cre-negative Floxed Myostatin mice (i.e., MSTN^{Flox/Flox}) were used as controls (referred to as Flox) in this study. The male Flox and BKO mice were established obesity model for 12-week 60% high-fat diet. After the obesity modeling period, the BAT, iWAT, liver and gastrocnemius tissues were collected for the examination of diet-induced obesity in Flox and BKO mice. To confirm the role of Myostatin in adaptive thermogenesis, mice were also subjected to

1 one-week 4°C cold stress, to detect the adaptive thermogenesis and browning
2 of iWAT.

3 **Animal experiment design 3#** To specifically over-expressed KLF4 in
4 BAT in vivo experiments, the adeno-associated virus serotype 8 (AAV8)-
5 encoding full-length KLF4 sequences (AAV-KLF4) delivery system was
6 established. After 12-weeks obesity modeling, AAV-KLF4 was injected to BAT.
7 After 3-weeks AAV injection, BAT, iWAT, liver and gastrocnemius samples were
8 collected from mice to detect corresponding histological, biochemical, and
9 molecular biological analysis.

10 **Animal experiment design 4#**

11 we crossed the Rosa26^{CAG-LSL-Cas9-tdTomato} mice with the UCP1-Cre
12 transgenic mice and obtained the UCP1-Cre; Rosa26^{CAG-LSL-Cas9-tdTomato} mice,
13 the male Rosa26^{CAG-LSL-Cas9-tdTomato} and UCP1-Cre; Rosa26^{CAG-LSL-Cas9-tdTomato}
14 male mice were established obesity model for 12-week 60% high-fat diet. Then
15 we constructed the adeno-associated virus of pAAV-U6-spgRNA (Mstn)-CMV-
16 EGFP-WPRE, and AAV-sgMstn was injected to BAT in situ to specifically
17 knockdown MSTN in BAT. Rosa26^{CAG-LSL-Cas9-tdTomato} mice (Strain NO.T002249)
18 were purchased from GemPharmatech (Nanjing, China)

19 **Animal experiment design 5#** To confirm whether FGF21 contributes to
20 the inflammation induced by Myostatin ablation, we established a delivery
21 system encoding the full-length FGF21 sequence (AAV-FGF21) of adeno-
22 associated virus type 8 (AAV8). After 12-weeks obesity modeling, AAV-FGF21
23 was injected into BAT in situ to specifically overexpress FGF21 in BAT. After 3-
24 weeks AAV injection, BAT, iWAT, liver and gastrocnemius samples were
25 collected from male mice to detect corresponding histological, biochemical and
26 molecular biological analysis.

27 **Animal experiment design 6#** To confirm whether FGF21 contributes to
28 the inflammation induced by Myostatin ablation, we injected rFGF21 direct into
29 BAT one-time of BKO mice. The dose of rFGF21 is 2mg/kg (53). Since the half-
30 life of recombinant FGF21 in rodents and primates has been determined to be
31 approximately 1-2 h (54). After one-time rFGF21 injection, the BAT, iWAT, liver
32 and gastrocnemius samples were collected within 2 hours.

33 **Body Composition Measurement**

34 The Minispec mq10 NMR Analyzer (Bruker) was used to measure the body
35 composition of mice according to the manufacturer's instructions. Briefly, mice
36 were put in an NMR tube and loaded in the NMR machine. The body
37 composition was measured automatically by the machine.

38 **Glucose and Insulin Tolerance Tests**

Glucose and insulin tolerance tests (GTT and ITT) were performed as previously described. Briefly, mice were fasted overnight before GTT. Glucose (1.5g/kg) was administered intraperitoneally (i.p.), and blood glucose levels were measured at 0, 15, 30, 60, and 120 min after injection. Mice were fasted for 6 hours before ITT. Insulin (0.8U/kg) was administered i.p., and blood glucose was measured at 0, 15, 30, 60, and 120 min after injection.

Body Temperature and Surface Temperature

Mice were hand-restrained, the rectal temperature was monitored by using animal digital electronic thermometer (ALC-ET03/06, ALCOTT BIOTECH, China). And a rectal probe was gently inserted into the rectum to a depth of 2 cm. To alleviate acute stress-induced increases in body temperature, the mice were trained in advance to the measurement procedure and to the restraint every day for three days. Infrared thermographic camera was used to collect mice surface temperature (FOTRIC 220s, China). For assessment of living mice, infrared thermographic camera placed vertically above the mouse and within less than 1 m distance from the animal. Each infrared digital image was analyzed with FOTRIC AnalyzIR software.

Cold Tolerance Test

To test tolerance to cold exposure, mice were individually housed at 4°C without bedding and with free access to food and water. The core body temperature of the mice was measured using a rectal thermometer at 0, 1, 2, 4, 6, 8 and 10h.

Muscle-grip strength test

In this study, the grip strength of mice was assessed using a grip strength meter. Prior to testing, mice underwent a two-day acclimatization period with the apparatus. For the measurement, each mouse was aligned with a metal grid, where it was allowed to grip with its four limbs. Subsequently, a gentle tail pull was applied until the mouse voluntarily released its grip. The grip strength was determined by averaging the results from three consecutive tests.

Treadmill performance test

For this test, mice underwent a two-day acclimation period on the treadmill apparatus. The test commenced with a 5-minute warm-up phase, during which the mice were subjected to a 10° incline and a constant speed of 10 meters per minute. Following the warm-up, the treadmill speed was incrementally increased by 2 meters per minute every 5 minutes. The endpoint of the test was defined as the point of exhaustion, determined by the mouse's inability to continue running.

Latency Measurement in the Mouse Sciatic Nerve-Gastrocnemius Muscle

System

Prior to the experiment, anesthesia was administered via intraperitoneal injection of pentobarbital, with dosage adjusted according to body weight. Under sterile conditions, a unilateral surgical exposure of the sciatic nerve was performed. A precision stimulator delivered a square wave pulse of fixed duration, with stimulus intensity controlled to elicit visible muscle responses without causing tissue damage. Latency periods of the gastrocnemius muscle were recorded using needle electrodes strategically placed in the muscle to detect the onset of contraction following nerve stimulation. Data were amplified and recorded using a standard electrophysiological recording system (55).

Preparation and delivery of Cardiotoxin

A working solution of 10 μ M was aliquoted into disposable Eppendorf vials. For muscle injury induction, sterilizing the area with 70% ethanol followed by the injection of about 50 μ L of the 10 μ M cardiotoxin into the TA muscle belly. The injection site was carefully chosen 1 cm below the proximal insertion of the TA, with the needle inserted at a shallow angle along the muscle belly and the syringe held at a 20° angle. In every case of cardiotoxin-induced injury, the contralateral leg was kept uninjured to serve as a control (56).

Energy Metabolism

Metabolic condition of mice that were 12-weeks HFD-fed was determined by using the TSE PhenoMaster Animal Monitoring System (TSE Systems Instruments). Body weight-matched mice were housed individually and maintained under a 12-hours light/12-hours dark cycle at 23°C with free access to food and water. Oxygen consumption, carbon dioxide production, respiratory exchange ratio, and energy expenditure were measured during the experiment. Data were analyzed by using CalR, a web-based analysis tool for indirect calorimetry experiments (57). Total body mass was used as a covariate.

Histology

BAT, iWAT, Liver, and GAS tissues were fixed in a 4% paraformaldehyde solution for 24 h, embedded in paraffin. Hematoxylin-eosin (H&E) (hematoxylin, E607317-0500; eosin, E607321-0100, Sangon Biotech, Shanghai, China) staining was performed on paraffin-embedded tissues to visualize the pattern of lipid accumulation. Oil Red O (E607319-0010; Sangon Biotech, Shanghai, China) staining was performed on optimal cutting temperature (OCT) compound (4583, Sakura, Torrance, CA)-embedded frozen liver or GAS sections to visualize lipid droplet accumulation. UCP1 (Abcam) staining was performed to detect BAT thermogenesis, and F4/80 (Proteintech) staining was performed to detect liver lobule inflammation. Histological features were

1 observed and captured with a light microscope (OLYMPUS DP80, Olympus,
2 Tokyo, Japan).

3 **Muscle fiber measurements**

4 Each image started by setting the actual dimensions using
5 "Analyze" > "Set Scale". To analyze muscle fiber cross-sectional area, select
6 the "Freehand selections" tool to manually outline the muscle fiber contours.
7 Once a muscle fiber is selected, choose "Analyze" > "Measure" to calculate and
8 display the area of the selected region. Repeat these steps for all muscle fibers.
9 The "ROI Manager" can be used to manage and label multiple regions,
10 facilitating the measurement process across multiple fibers. During the process
11 of muscle fiber measurements, three mice for each group and for each mouse,
12 ranging from 1000-3000 muscle fibers were included in the calculation.

13 **Immunofluorescence**

14 In immunohistochemical analyses, 20 μ m sections were prepared. Primary
15 antibodies targeting MyHC-I (BA-D5), MyHC-IIa (SC-71), and MyHC-IIb (BF-
16 F3) were procured from Developmental Studies Hybridoma Bank (DSHB, Iowa,
17 USA). Secondary antibodies, namely Alexa Fluor 350 anti-mouse IgG2b (A-
18 21140), Alexa Fluor 488 anti-mouse IgG1 (A-21121), and Alexa Fluor 555 anti-
19 mouse IgM (A-21426), were sourced from Thermo Fisher. Imaging was
20 conducted using a Zeiss confocal microscope, with quantitative assessments
21 performed via Fiji software.

22 **Electron microscopy**

23 BAT and GAS of 12-week HFD-fed BKO and Flox mice were fixed as
24 previously described (58). Ultrathin sections of BAT and muscles were prepared
25 by ultramicrotome (Leica EM UC7) and the grids were analyzed with a JEM-
26 2100 transmission electron microscope (Hitachi HT7700, Japan).

27 **Measurement of Lipids**

28 Tissue lipids were extracted with chloroform and methanol and determined
29 as previously described (59). The TG content in the plasma, liver and GAS
30 tissues was measured as recommended by the manufacturer (Sigma, TR0100).
31 The absorbance at 540 nm was measured with a microporous plate
32 spectrophotometer (Spark, Switzerland).

33 **Muscle fibers permeabilization and mitochondrial respiration studies**

34 GAS muscles were excised, segmented into 15–20 mg pieces, and
35 immediately submerged in ice-cold BIOPS solution. Fiber bundles were
36 delicately dissected, saponin-treated, and agitated in BIOPS. Subsequently,
37 fibers were swiftly transferred to MIR05 solution. Permeabilized fibers, weighing
38 2-3 mg in total, were introduced into O2K chambers. Upon excision of BAT, a
39 swift procedure is followed where a small section, approximately 2 mg in weight,
40 is rapidly excised. After adequate grinding, the resultant tissue suspension is

collected and subsequently deposited into the O2K chamber for analysis. Maximal respiration flux was assessed using substrates including 5 mM pyruvate, 2 mM malate, 10 mM glutamate, and 2.5 mM ADP. Additionally, cytochrome c at a concentration of 10 mM was employed to assess the integrity of the mitochondrial outer membrane. 0.5 μ M Rotenone was utilized for isolating respiration through complex I, 1M succinate for complex II, and a solution of 2.5 μ M antimycin A with for complex III analysis.

Sequence Alignment and Gene Expression Analysis

The BAT and muscle tissue samples from each group were collected for RNA sequencing. Total RNA was isolated using the Trizol method following the manufacturer's instructions. The quality of the RNA was assessed using the Agilent 2100 Bioanalyzer with the RNA 6000 Nano Kit from Agilent Technologies, Santa Clara, CA, USA. cDNA libraries for each sample were constructed as previously described (60). The libraries were sequenced on the BGISEQ500 platform (BGI-Shenzhen, China) using 150 bp paired-end reads with a target of 30 million reads per sample. The raw sequencing data was filtered using trim-galore (v0.6.7) to remove reads containing sequencing adapters and low-quality bases. The resulting clean reads were aligned to the reference genome (mm10) using STAR (v2.5.2b). Gene expression quantification was performed using RSEM (v1.2.28) with commands `rsem-calculate-expression --paired-end -p 20 -alignments samples.bam star_index.files`. Differential gene expression analysis was conducted to compare MSTN Δ UCP1 to MSTN^{Flox/Flox}. DESeq2 (v1.42.0) was used for differential expression analysis, considering genes with an adjusted P value < 0.05 and |FC| > 1.5 as significant. Furthermore, KEGG pathway analysis was conducted using differentially expressed genes in, while gene-set enrichment analysis was performed using the obtained log₂FC values to detect pathways enriched with profiling genes.

UPLC-MS/MS lipid profiling

Serum samples were thawed using an ice bath to minimize sample degradation. For lipid extraction, 10 μ L of serum was dispensed into individual wells of a 96-well plate. Subsequently, 300 μ L of extraction solution was introduced into each well. The plate underwent vortexing for a duration of 20 minutes, followed by centrifugation at 4000g for 20 minutes (Allegra X-15R, Beckman Coulter, Inc., Indianapolis, IN, USA). Subsequently to centrifugation, 20 μ L of supernatant was carefully transferred to a fresh 96-well plate and combined with 80 μ L of dilution solution. The resultant mixture was securely sealed, and the plate was prepared for the ultra-performance liquid

1 chromatography coupled to tandem mass spectrometry (UPLC-MS/MS)
2 analysis. The UPLC-MS/MS system was employed for the precise
3 quantification of all targeted metabolites.

4 Lipid profiling was conducted using Waters ACQUITY UPLC system in
5 conjunction with a Waters XEVO TQ-S MS, controlled by MassLynx 4.1
6 software (Waters, Milford, MA). Chromatographic separation was achieved
7 utilizing an ACQUITY BEH C18 column (1.7 μ m, 100 mm by 2.1 mm internal
8 dimensions) (Waters, Milford, MA). The gradient elution commenced at a flow
9 rate of 0.4 ml/min, with an injected volume of 5 μ l and the column temperature
10 set at 40°C. Both mobile phases A and B comprised 5 mM ammonium formate
11 in a solution of A [acetonitrile/H₂O (95:5, v/v)] and B [acetonitrile/isopropanol
12 (10:90, v/v)], respectively.

13 The elution of lipids followed the specified gradients: 0 to 2 min, 60% B; 2
14 to 8 min, 60 to 100% B; 8 to 10 min, 100% B; and 10 to 12 min, 60% B. In the
15 ESI+ mode, the capillary voltage was set at 3.2 kV. The desolvation gas flow
16 was maintained at 1000 liters/hour. The electrospray ion source temperature
17 and desolvation temperature were held at 150 °C and 500 °C, respectively.
18 Selected lipids were detected using the multiple reaction monitoring mode with
19 specified precursor and product ions, as previously described (61). The
20 integration and quantification of raw lipid data generated by UPLC-Triple
21 Quadrupole Mass Spectrometry were executed using the TargetLynx
22 application manager (version 4.1, Waters, Milford, MA, USA).

23 **Cell Lines, Culture Conditions, and transfection**

24 Human HEK293T cells, and mouse macrophage were cultured in DMEM/H
25 (Gibco) with 10% fetal bovine serum (FBS, Gibco), 2mM L-glutamine (Gibco),
26 and 1% penicillin-streptomycin (P/S, Gibco), in a 5% CO₂ atmosphere at 37°C.
27 Polyethylenimine (PolySciences, 23966) was used for transfecting according to
28 the instructions of manufacturer.

29 **Isolation and Differentiation of primary brown adipocytes**

30 The interscapular BAT was dissected from male mice (10-14 days), minced
31 and digested for 30min at 37°C in isolation buffer (PBS containing 4% fatty-
32 acid-free BSA and 10 mg/ml collagenase D (Roche)). Digested tissue was
33 filtered through a 100 μ m cell strainer to remove large pieces, and the flow-
34 through was then centrifuged for 10 min at 600x g to collect the supernatant
35 (mature adipocytes) and sediment (stromal vascular fraction cells). Then the
36 sediment re-suspended cells and transferred to cell culture dishes.
37 Differentiation of brown adipocytes was as previously described (62). To
38 determine effect of SMAD2/3 and p38 signaling pathway, 10 μ M p38 inhibitor,

20nM SMAD2/3 inhibitor, 1 μ M p38 agonist (MedChemExpress, SB202190, Dehydrocorydaline or TP0427736 HCl, China) or 20nM rMSTN (ACMEC biochemical, AC13218) were used to treat primary brown adipocytes.

Co-culture assay

To simulate the in vivo environment of obese mice, macrophage was induced inflammation by 200 nM palmitic acid (Sigma) (63). Macrophage cells was first induced with palmitic acid for 24 hours, then cocultured with mature adipocytes or BAT from Flox and BKO mice with/without rFGF21 protein for 24 hours. Finally, the cells were harvested for indicated experiments. The concentration of rFGF21 protein (MCE, China) was according to previously described (26).

Western blotting

Proteins were extracted with RIPA buffer (Beyotime Biotechnology, China)) containing protease and phosphatase inhibitors (Beyotime Biotechnology, China) and were quantified using Rapid BCA Protein Assay Kit (Thermo Fisher, USA) according to the manufacturer's instructions. Western blot analysis was performed as previous described (64). Briefly, 30 μ g lysate was loaded onto SDS-PAGE gels, blotted onto polyvinylidene difluoride (PVDF) membranes (Millipore, USA), and incubated with antibodies. The primary antibodies used in this work including anti-MSTN (R&D systems, AF788), anti-KLF4 (Abclonal, A13673), anti-PGC1 α (Novus, NBP1-04676), anti-UCP1 (Abcam, ab10983), anti-LC3B (Sigma, L7543), anti-p62 (Proteintech, 18420-1-AP), anti-PINK1 (Santa, sc-517353), anti-ATP5A (Abcam, ab14748), anti-ATP5A (Abcam, ab14748), anti-SDHB (Proteintech, 10620-1-AP), anti-NDUFB8 (Proteintech, 14794-1-AP), anti-p62 (Proteintech, 18420-1-AP), anti- Phospho-SMAD2/3 (CST, 8828S), anti-SMAD2/3 (CST, 8685S), anti- Phospho-p38 (CST, 9211S), anti-p38 (CST, 9212S), anti- Phospho-ERK (CST, 9101S), anti-ERK (CST, 9102S), anti- Phospho-JNK (CST, 9251S), anti-JNK (CST, 9252S), anti-FGF21 (Abclonal, A23463), anti- β -Tubulin (Abclonal, AC008), anti-GAPDH (Abways, AB0037).

Analysis of Gene Expression by Quantitative Real-Time PCR

TRIzol method (Thermo Fisher) was used to extract total RNA from tissues and cells according to the manufacturer's instructions. Briefly, 1 μ g RNA was converted into cDNA using High-Capacity cDNA Reverse Transcription Kit (Thermo Fisher), and QPCR was performed with a QuantStudio™ 7 Flex Real-Time PCR System (Thermo Fisher) using SYBR Green PCR Master Mix (ACCURATE BIOTECHNOLOGY) according to the manufacturer's instructions. Tbp, 36b4 or beta-actin was used as the endogenous control. The primers list

was shown in Table 1.

Mitochondrial DNA Copy Number

Mitochondrial DNA (mtDNA) copy number was determined via quantitative RT-PCR as previously described (6). Briefly, total DNA was isolated from the BAT using Mouse Direct PCR Kit (Bimake, B40015) according to the manufacturer's instructions. The mtDNA copy number was calculated from the ratio of COX II (mitochondrial-encoded gene) to cyclophilin A (nuclear-encoded gene).

Chromatin immunoprecipitation (ChIP)-qPCR assay

By using the website <https://jaspar.elixir.no/>, we predicted there were 8 potential KLF4 binding elements on the Pink1 promoter. We performed the ChIP assay using the Sonication chip Kit (ABclonal, China), according to the manufacturer's instructions. In brief, we fixed 1×10^6 primary brown adipocytes in 1% formaldehyde for 10 min at ambient temperature. The fixed cells were harvested, lysed, and sonicated for 35 cycles of 20s ON/30s OFF and 30% AMPL using SONICS VCX130 (SONICS, USA). Antibodies against KLF4 (Proteintech, 11880-1-AP, China) and rabbit IgG (ABclonal, China) were used for immunoprecipitation. PCR amplification of the precipitated DNA was performed. The primer sequences were used for the ChIP assay as followed (Table 1).

Table 1 ChIP assay primer list

Predicted site	Forward primer	Reverse primer
-470/-461	GGGACCCACATGAAGGCA	TGGGTCGTGGGGATCAAACCTC
-561/-552	GGGACCCACATGAAGGCA	TGGGTCGTGGGGATCAAACCTC
-605/-596	GAGCCTGTCTATACAGGCA	CCCATGAACAGGGAGTGAA
-671/-662	CATGTAGCAAAGATGCAGC	CTTACCAGACCTGCCCTTGCA
-887/-878	TACTCCTCTCAGCCCAGCA	AATAGGCTGAAGCCAGGCCCA
-931/-922	TCACACCCCTTGCTCTTCAC	TGCTGGGACACCTCTGTCA
-1186/-1177	GCTGGGTGGGCAGGAGTCA	CCCTCCTGAGCTGTTCAAGG

Plasmids Construction and Lentivirus Infection

Encoding small hairpin RNA targeting MSTN, was constructed by inserting small hairpin RNA sequence (CCGGCCTTTGGATGGGACTGGATTACTCGAGTAATCCAGTCCCATCCAAAGGTTTTT G (F) and AATTCAAAAACCTTTGGATGGGACTGGATTACTCGAGTAATCCAGTCCCA TCCAAAGG (R)) into the AgeI/EcoRI site of pLKO.1-puro (Addgene). And packaging constructed shRNA of MSTN into lentivirus. When the primary brown

adipocytes reach 60% confluence, they can be infected with lentivirus for knockdown Mstn. pCDNA3.1-KLF4 was constructed by amplifying PCR products from C57BL/6J mouse cDNA and inserting into the EcoRI/XbaI site of pcDNA3.1 (OBiO Technology).

AAV-KLF4 Production and Injection

pAAV-CMV-KLF4-3xFLAG-EF1-mNeonGreen-tWPA, pAAV-CMV-FGF21-3xFLAG-EF1-GdGreen-WPRE, pAAV-U6-spgRNA (Mstn)-CMV-EGFP-WPRE was produced and purified by OBiO Technology. For KLF4 and FGF21 expression experiment in vivo, a dose of 1.3×10^{11} GC of AAV-KLF4 was in situ injected into the interscapular BAT of BKO mice and a same dose of AAV-GFP was in situ injected into the interscapular BAT of Flox mice on 8-week HFD. GTT and ITT were performed after 3-4 weeks of virus injection, respectively. For Myostatin knockout experiment in vivo, a dose of 1.3×10^{11} GC of AAV8-sgMstn was in situ injected into the interscapular BAT of UCP1-Cre; Cas9 mice and the same dose of AAV8-sgCon was in situ injected into the interscapular BAT of Cas9 mice.

Statistical Analysis

The correlation between the expression of MSTN in subcutaneous fat and BMI and HOMA-IR was calculated by Spearman's rank correlation coefficient. A two-tailed Student t test was performed for comparison of two groups. One-way ANOVA followed by Bonferroni post-tests were performed for intergroup comparisons. All data were presented as mean \pm standard error of mean (SEM).

The lipid profiling analyses were performed in the R environment. A partial least squares-discriminant analysis (PLS-DA) model was constructed using R packages "mixOmics". The t tests were used to analyze the significance of the metabolites between the groups. $p < 0.05$ was considered to be significant. The heatmap was constructed using R packages "Complex Heatmap".

Study approval

All animal studies were approved by the Institutional Animal Care and Use Committee of Shanghai university of sport (102772022DW020).

Data and Software Availability

The accession number for the RNA-Seq data reported in this paper is GEO: GSE249030. All bioinformatics software used in the study are publicly available. All remaining data that support the findings of this study are available in the main text or the supplemental materials. See the Supplemental Supporting Data Values file for values underlying the data presented in each graph and as means in the figures.

Author contributions

X.K. and T.L. designed research; H. W., S. G., J. D., XY. K., S.Z., Y.F., M.H., H.Z., W.W., H.L., K.X., and H.G. performed experiments; H.W., Y.C. and Y.F.

1 performed bioinformatics and metabolomics analysis. T.L., S.G., X.K. analyzed
2 data; and X.K. wrote the paper. All authors reviewed and contributed to the
3 manuscript.

4 **Acknowledgments**

5 The authors acknowledge the assistance of the platform of State Key
6 Laboratory of Genetic Engineering at Fudan University. This work was funded
7 by the National Natural Science Foundation of China (92157203) to X.K.; the
8 National Key R&D Program of China (2019YFA0801900,2018YFA0800300),
9 the National Natural Science Foundation of China (92357304,92249302),
10 Faculty Resources Project of College of Life Sciences, Inner Mongolia
11 University (2022-102) to T.L.; the National Natural Science Foundation of China
12 (32371194) to H.G.; the National Natural Science Foundation of China
13 (8230034352) to Y.F.; the National Natural Science Foundation of China
14 (82000790) to W.W..

15 **Competing interests**

16 The authors declare no competing interest.

Reference

1. Carpentier AC, Blondin DP, Haman F, and Richard D. Brown Adipose Tissue-A Translational Perspective. *Endocr Rev.* 2023;44(2):143-92.
2. Aquilano K, Zhou B, Brestoff JR, and Lettieri-Barbato D. Multifaceted mitochondrial quality control in brown adipose tissue. *Trends Cell Biol.* 2022.
3. Yin X, Chen Y, Ruze R, Xu R, Song J, Wang C, et al. The evolving view of thermogenic fat and its implications in cancer and metabolic diseases. *Signal Transduct Target Ther.* 2022;7(1):324.
4. Villarroya F, Cereijo R, Villarroya J, and Giralt M. Brown adipose tissue as a secretory organ. *Nat Rev Endocrinol.* 2017;13(1):26-35.
5. Li P, Fan C, Cai Y, Fang S, Zeng Y, Zhang Y, et al. Transplantation of brown adipose tissue up-regulates miR-99a to ameliorate liver metabolic disorders in diabetic mice by targeting NOX4. *Adipocyte.* 2020;9(1):57-67.
6. Kong X, Yao T, Zhou P, Kazak L, Tenen D, Lyubetskaya A, et al. Brown Adipose Tissue Controls Skeletal Muscle Function via the Secretion of Myostatin. *Cell Metab.* 2018;28(4):631-43 e3.
7. McPherron AC, Lawler AM, and Lee SJ. Regulation of skeletal muscle mass in mice by a new TGF-beta superfamily member. *Nature.* 1997;387(6628):83-90.
8. Lee SJ. Targeting the myostatin signaling pathway to treat muscle loss and metabolic dysfunction. *J Clin Invest.* 2021;131(9).
9. Sivakumar K, Cochrane TI, Sloth B, Ashar H, Laurent D, Tanko LB, et al. Long-term safety and tolerability of bimagrumab (BYM338) in sporadic inclusion body myositis. *Neurology.* 2020;95(14):e1971-e8.
10. Polkey MI, Praestgaard J, Berwick A, Franssen FME, Singh D, Steiner MC, et al. Activin Type II Receptor Blockade for Treatment of Muscle Depletion in Chronic Obstructive Pulmonary Disease. A Randomized Trial. *Am J Respir Crit Care Med.* 2019;199(3):313-20.
11. Heymsfield SB, Coleman LA, Miller R, Rooks DS, Laurent D, Petricoul O, et al. Effect of Bimagrumab vs Placebo on Body Fat Mass Among Adults With Type 2 Diabetes and Obesity: A Phase 2 Randomized Clinical Trial. *JAMA Netw Open.* 2021;4(1):e2033457.
12. Rooks D, Swan T, Goswami B, Filosa LA, Bunte O, Panchaud N, et al. Bimagrumab vs Optimized Standard of Care for Treatment of Sarcopenia in Community-Dwelling Older Adults: A Randomized Clinical Trial. *JAMA Netw Open.* 2020;3(10):e2020836.
13. Becker C, Lord SR, Studenski SA, Warden SJ, Fielding RA, Recknor CP, et al. Myostatin antibody (LY2495655) in older weak fallers: a proof-of-concept, randomised, phase 2 trial. *Lancet Diabetes Endocrinol.* 2015;3(12):948-57.

- 1 14. Zhang C, McFarlane C, Lokireddy S, Masuda S, Ge X, Gluckman PD,
2 et al. Inhibition of myostatin protects against diet-induced obesity by
3 enhancing fatty acid oxidation and promoting a brown adipose
4 phenotype in mice. *Diabetologia*. 2012;55(1):183-93.
- 5 15. McPherron AC, and Lee SJ. Suppression of body fat accumulation in
6 myostatin-deficient mice. *J Clin Invest*. 2002;109(5):595-601.
- 7 16. LeBrasseur NK, Schelhorn TM, Bernardo BL, Cosgrove PG, Loria PM,
8 and Brown TA. Myostatin inhibition enhances the effects of exercise on
9 performance and metabolic outcomes in aged mice. *J Gerontol A Biol*
10 *Sci Med Sci*. 2009;64(9):940-8.
- 11 17. Akpan I, Goncalves MD, Dhir R, Yin X, Pistilli EE, Bogdanovich S, et al.
12 The effects of a soluble activin type IIB receptor on obesity and insulin
13 sensitivity. *Int J Obes (Lond)*. 2009;33(11):1265-73.
- 14 18. Amor M, Itariu BK, Moreno-Viedma V, Keindl M, Jurets A, Prager G, et
15 al. Serum Myostatin is Upregulated in Obesity and Correlates with
16 Insulin Resistance in Humans. *Exp Clin Endocrinol Diabetes*.
17 2019;127(8):550-6.
- 18 19. Singh R, Braga M, and Pervin S. Regulation of brown adipocyte
19 metabolism by myostatin/follistatin signaling. *Front Cell Dev Biol*.
20 2014;2:60.
- 21 20. Feldman BJ, Streeper RS, Farese RV, Jr., and Yamamoto KR.
22 Myostatin modulates adipogenesis to generate adipocytes with
23 favorable metabolic effects. *Proc Natl Acad Sci U S A*.
24 2006;103(42):15675-80.
- 25 21. Birsoy K, Chen Z, and Friedman J. Transcriptional regulation of
26 adipogenesis by KLF4. *Cell Metab*. 2008;7(4):339-47.
- 27 22. Rosencrans WM, Walsh ZH, Houerbi N, Blum A, Belew M, Liu C, et al.
28 Cells deficient for Kruppel-like factor 4 exhibit mitochondrial dysfunction
29 and impaired mitophagy. *Eur J Cell Biol*. 2020;99(1):151061.
- 30 23. Chen Z, Yang L, Liu Y, Huang P, Song H, and Zheng P. The potential
31 function and clinical application of FGF21 in metabolic diseases. *Front*
32 *Pharmacol*. 2022;13:1089214.
- 33 24. Larsson SC, Michaelsson K, Mola-Caminal M, Hoijer J, and Mantzoros
34 CS. Genome-wide association and Mendelian randomization study of
35 fibroblast growth factor 21 reveals causal associations with
36 hyperlipidemia and possibly NASH. *Metabolism*. 2022;137:155329.
- 37 25. Geng L, Lam KSL, and Xu A. The therapeutic potential of FGF21 in
38 metabolic diseases: from bench to clinic. *Nat Rev Endocrinol*.
39 2020;16(11):654-67.
- 40 26. Fisher FM, Kleiner S, Douris N, Fox EC, Mepani RJ, Verdeguer F, et al.
41 FGF21 regulates PGC-1alpha and browning of white adipose tissues in
42 adaptive thermogenesis. *Genes Dev*. 2012;26(3):271-81.
- 43 27. Huang Z, Zhong L, Lee JTH, Zhang J, Wu D, Geng L, et al. The
44 FGF21-CCL11 Axis Mediates Beiging of White Adipose Tissues by

- 1 Coupling Sympathetic Nervous System to Type 2 Immunity. *Cell Metab.*
2 2017;26(3):493-508 e4.
- 3 28. Steculorum SM, Ruud J, Karakasilioti I, Backes H, Engstrom Ruud L,
4 Timper K, et al. AgRP Neurons Control Systemic Insulin Sensitivity via
5 Myostatin Expression in Brown Adipose Tissue. *Cell.* 2016;165(1):125-
6 38.
- 7 29. Jackson MF, Li N, and Rodgers BD. Myostatin regulates tissue potency
8 and cardiac calcium-handling proteins. *Endocrinology.*
9 2014;155(5):1771-85.
- 10 30. Garcia-Retortillo S, Romero-Gomez C, and Ivanov PC. Network of
11 muscle fibers activation facilitates inter-muscular coordination, adapts
12 to fatigue and reflects muscle function. *Commun Biol.* 2023;6(1):891.
- 13 31. Wang Y, Lu J, and Liu Y. Skeletal Muscle Regeneration in Cardiotoxin-
14 Induced Muscle Injury Models. *Int J Mol Sci.* 2022;23(21).
- 15 32. Bergman BC, and Goodpaster BH. Exercise and Muscle Lipid Content,
16 Composition, and Localization: Influence on Muscle Insulin Sensitivity.
17 *Diabetes.* 2020;69(5):848-58.
- 18 33. Lu Y, Fujioka H, Joshi D, Li Q, Sangwung P, Hsieh P, et al. Mitophagy
19 is required for brown adipose tissue mitochondrial homeostasis during
20 cold challenge. *Sci Rep.* 2018;8(1):8251.
- 21 34. Shan T, Liang X, Bi P, and Kuang S. Myostatin knockout drives
22 browning of white adipose tissue through activating the AMPK-
23 PGC1alpha-Fndc5 pathway in muscle. *FASEB J.* 2013;27(5):1981-9.
- 24 35. Liao X, Zhang R, Lu Y, Prosdocimo DA, Sangwung P, Zhang L, et al.
25 Kruppel-like factor 4 is critical for transcriptional control of cardiac
26 mitochondrial homeostasis. *J Clin Invest.* 2015;125(9):3461-76.
- 27 36. Jin L, Ye H, Pan M, Chen Y, Ye B, Zheng Y, et al. Kruppel-like factor 4
28 improves obesity-related nephropathy through increasing mitochondrial
29 biogenesis and activities. *J Cell Mol Med.* 2020;24(2):1200-7.
- 30 37. Liao X, Sharma N, Kapadia F, Zhou G, Lu Y, Hong H, et al. Kruppel-like
31 factor 4 regulates macrophage polarization. *J Clin Invest.*
32 2011;121(7):2736-49.
- 33 38. Bulut GB, Alencar GF, Owsiany KM, Nguyen AT, Karnewar S, Haskins
34 RM, et al. KLF4 (Kruppel-Like Factor 4)-Dependent Perivascular
35 Plasticity Contributes to Adipose Tissue inflammation. *Arterioscler*
36 *Thromb Vasc Biol.* 2021;41(1):284-301.
- 37 39. Huang Z, Chen X, and Chen D. Myostatin: a novel insight into its role in
38 metabolism, signal pathways, and expression regulation. *Cell Signal.*
39 2011;23(9):1441-6.
- 40 40. Li HX, Han M, Bernier M, Zheng B, Sun SG, Su M, et al. Kruppel-like
41 factor 4 promotes differentiation by transforming growth factor-beta
42 receptor-mediated Smad and p38 MAPK signaling in vascular smooth
43 muscle cells. *J Biol Chem.* 2010;285(23):17846-56.
- 44 41. Quesada-Lopez T, Cereijo R, Turatsinze JV, Planavila A, Cairo M,

- 1 Gavalda-Navarro A, et al. The lipid sensor GPR120 promotes brown fat
2 activation and FGF21 release from adipocytes. *Nat Commun*.
3 2016;7:13479.
- 4 42. Xu P, Zhang Y, Liu Y, Yuan Q, Song L, Liu M, et al. Fibroblast growth
5 factor 21 attenuates hepatic fibrogenesis through TGF-beta/smad2/3
6 and NF-kappaB signaling pathways. *Toxicol Appl Pharmacol*.
7 2016;290:43-53.
- 8 43. Luo X, Zhang H, Cao X, Yang D, Yan Y, Lu J, et al. Endurance
9 Exercise-Induced Fgf21 Promotes Skeletal Muscle Fiber Conversion
10 through TGF-beta1 and p38 MAPK Signaling Pathway. *Int J Mol Sci*.
11 2023;24(14).
- 12 44. Lin S, Yu L, Ni Y, He L, Weng X, Lu X, et al. Fibroblast Growth Factor
13 21 Attenuates Diabetes-Induced Renal Fibrosis by Negatively
14 Regulating TGF-beta-p53-Smad2/3-Mediated Epithelial-to-
15 Mesenchymal Transition via Activation of AKT. *Diabetes Metab J*.
16 2020;44(1):158-72.
- 17 45. Guo T, Jou W, Chanturiya T, Portas J, Gavrilova O, and McPherron AC.
18 Myostatin inhibition in muscle, but not adipose tissue, decreases fat
19 mass and improves insulin sensitivity. *PLoS One*. 2009;4(3):e4937.
- 20 46. Lee SJ. Sprinting without myostatin: a genetic determinant of athletic
21 prowess. *Trends Genet*. 2007;23(10):475-7.
- 22 47. Fedorenko A, Lishko PV, and Kirichok Y. Mechanism of fatty-acid-
23 dependent UCP1 uncoupling in brown fat mitochondria. *Cell*.
24 2012;151(2):400-13.
- 25 48. Lee SJ, and McPherron AC. Regulation of myostatin activity and
26 muscle growth. *Proc Natl Acad Sci U S A*. 2001;98(16):9306-11.
- 27 49. Hirosumi J, Tuncman G, Chang L, Gorgun CZ, Uysal KT, Maeda K, et
28 al. A central role for JNK in obesity and insulin resistance. *Nature*.
29 2002;420(6913):333-6.
- 30 50. Sabio G, Das M, Mora A, Zhang Z, Jun JY, Ko HJ, et al. A stress
31 signaling pathway in adipose tissue regulates hepatic insulin
32 resistance. *Science*. 2008;322(5907):1539-43.
- 33 51. Aouadi M, Laurent K, Prot M, Le Marchand-Brustel Y, Binetruy B, and
34 Bost F. Inhibition of p38MAPK increases adipogenesis from embryonic
35 to adult stages. *Diabetes*. 2006;55(2):281-9.
- 36 52. Crespo M, Nikolic I, Mora A, Rodriguez E, Leiva-Vega L, Pintor-
37 Chocano A, et al. Myeloid p38 activation maintains macrophage-liver
38 crosstalk and BAT thermogenesis through IL-12-FGF21 axis.
39 *Hepatology*. 2023;77(3):874-87.
- 40 53. Kang K, Xu P, Wang M, Chunyu J, Sun X, Ren G, et al. FGF21
41 attenuates neurodegeneration through modulating neuroinflammation
42 and oxidant-stress. *Biomed Pharmacother*. 2020;129:110439.
- 43 54. Kharitonov A, Wroblewski VJ, Koester A, Chen YF, Clutinger CK,
44 Tigno XT, et al. The metabolic state of diabetic monkeys is regulated by

- 1 fibroblast growth factor-21. *Endocrinology*. 2007;148(2):774-81.
- 2 55. Zheng H, Zhang Z, Jiang S, Yan B, Shi X, Xie Y, et al. A shape-memory
- 3 and spiral light-emitting device for precise multisite stimulation of nerve
- 4 bundles. *Nat Commun*. 2019;10(1):2790.
- 5 56. Garry GA, Antony ML, and Garry DJ. Cardiotoxin Induced Injury and
- 6 Skeletal Muscle Regeneration. *Methods Mol Biol*. 2016;1460:61-71.
- 7 57. Mina AI, LeClair RA, LeClair KB, Cohen DE, Lantier L, and Banks AS.
- 8 CalR: A Web-Based Analysis Tool for Indirect Calorimetry Experiments.
- 9 *Cell Metab*. 2018;28(4):656-66 e1.
- 10 58. Yao T, Yan H, Zhu X, Zhang Q, Kong X, Guo S, et al. Obese Skeletal
- 11 Muscle-Expressed Interferon Regulatory Factor 4 Transcriptionally
- 12 Regulates Mitochondrial Branched-Chain Aminotransferase
- 13 Reprogramming Metabolome. *Diabetes*. 2022;71(11):2256-71.
- 14 59. Jaeger D, Schoiswohl G, Hofer P, Schreiber R, Schweiger M,
- 15 Eichmann TO, et al. Fasting-induced G0/G1 switch gene 2 and FGF21
- 16 expression in the liver are under regulation of adipose tissue derived
- 17 fatty acids. *J Hepatol*. 2015;63(2):437-45.
- 18 60. Feng Y, Cui Z, Lu X, Gong H, Liu X, Wang H, et al. Transcriptomics
- 19 Dissection of Calorie Restriction and Exercise Training in Brown
- 20 Adipose Tissue and Skeletal Muscle. *Nutrients*. 2023;15(4).
- 21 61. Butera A, Agostini M, Cassandri M, De Nicola F, Fanciulli M,
- 22 D'Ambrosio L, et al. ZFP750 affects the cutaneous barrier through
- 23 regulating lipid metabolism. *Sci Adv*. 2023;9(17):eadg5423.
- 24 62. Galmozzi A, Kok BP, and Saez E. Isolation and Differentiation of
- 25 Primary White and Brown Preadipocytes from Newborn Mice. *J Vis*
- 26 *Exp*. 2021(167).
- 27 63. Guo S, Feng Y, Zhu X, Zhang X, Wang H, Wang R, et al. Metabolic
- 28 crosstalk between skeletal muscle cells and liver through IRF4-FSTL1
- 29 in nonalcoholic steatohepatitis. *Nat Commun*. 2023;14(1):6047.
- 30 64. Zhu X, Yao T, Wang R, Guo S, Wang X, Zhou Z, et al. IRF4 in Skeletal
- 31 Muscle Regulates Exercise Capacity via PTG/Glycogen Pathway. *Adv*
- 32 *Sci (Weinh)*. 2020;7(19):2001502.
- 33
- 34
- 35
- 36
- 37
- 38
- 39
- 40
- 41
- 42
- 43
- 44

Figure Legends

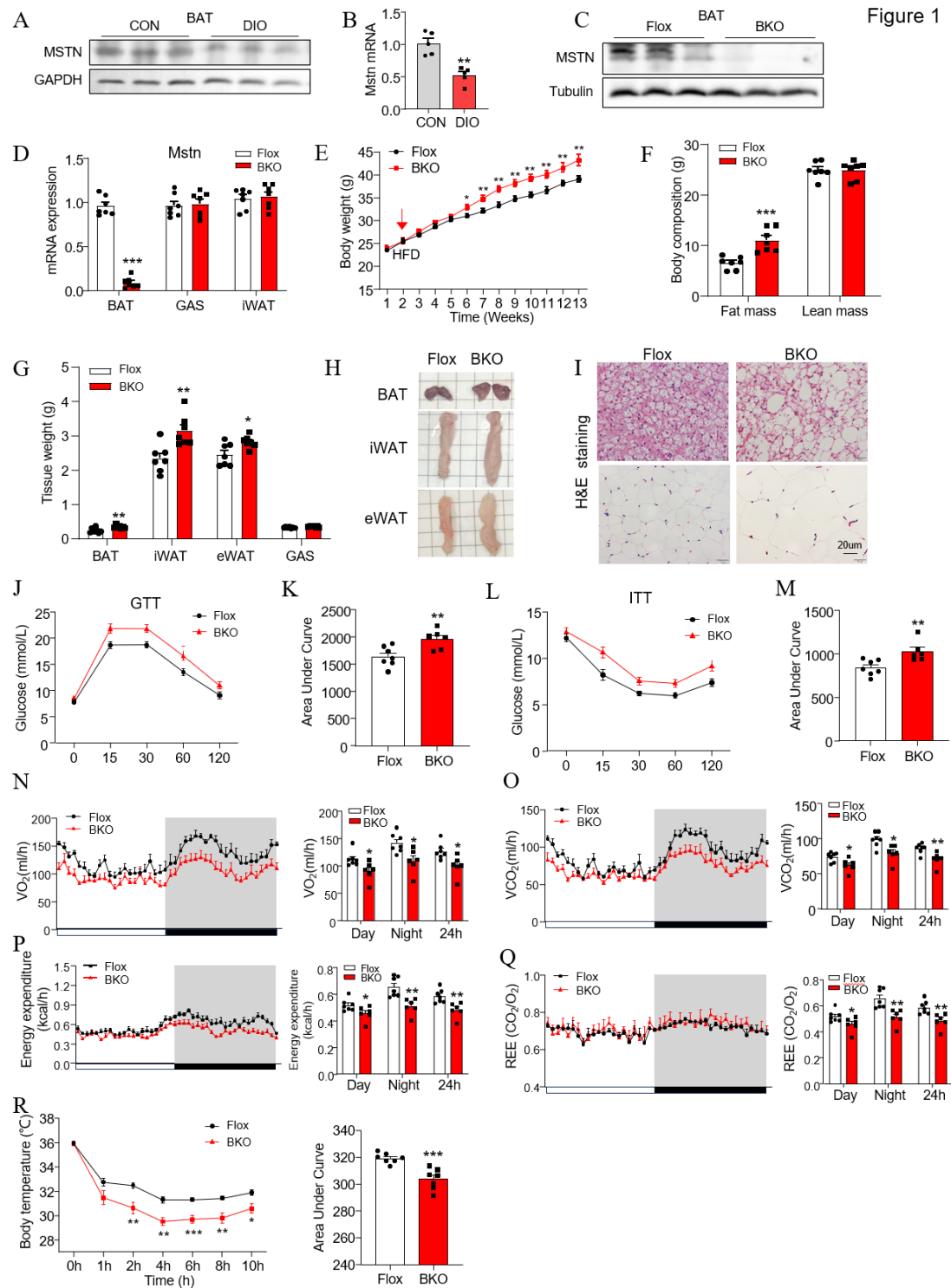


Figure 1. Mice with BAT specific MSTN knockout are prone to diet-induced obesity (DIO). **(A)** Western blot analysis of the expression of MSTN in BAT of DIO mice (n=3). **(B)** The mRNA expression of *mstn* in BAT of DIO mice (n= 5). **(C)** Western blot analysis of the expression of MSTN in BAT of male BKO and

1 Flox mice on 12-week HFD (n= 3). **(D)** The mRNA expression of mstn in BAT,
2 GAS and iWAT of male BKO and Flox mice on 12-week HFD (n= 7). **(E)** The
3 body weight of male BKO and Flox mice on HFD (n= 7-10). **(F)** The body
4 composition of male BKO and Flox mice on HFD (n= 7). **(G)** The weight of BAT,
5 iWAT, eWAT and GAS from male BKO and Flox mice on 12-week HFD (n= 7).
6 **(H)** The morphology of BAT, iWAT, eWAT. **(I)** H&E staining of BAT, iWAT of male
7 BKO and Flox mice on 12-week HFD (scale bars, 50µm). **(J-M)** The glucose
8 tolerance test (GTT) and insulin tolerance test (ITT) in male BKO and Flox mice
9 (n= 6-7). **(N-Q)** The oxygen consumption, carbon dioxide production, energy
10 expenditure, and respiratory exchange ratio of male BKO and Flox mice on 12-
11 week HFD (n= 6-7). **(R)** The body temperature of male BKO and Flox mice
12 during cold challenges (n= 7). All results were shown as mean ± SEM. * $p<0.05$,
13 ** $p<0.01$, *** $p<0.001$. A two-tailed Student *t* test was used for statistical analysis.
14
15

Figure 2

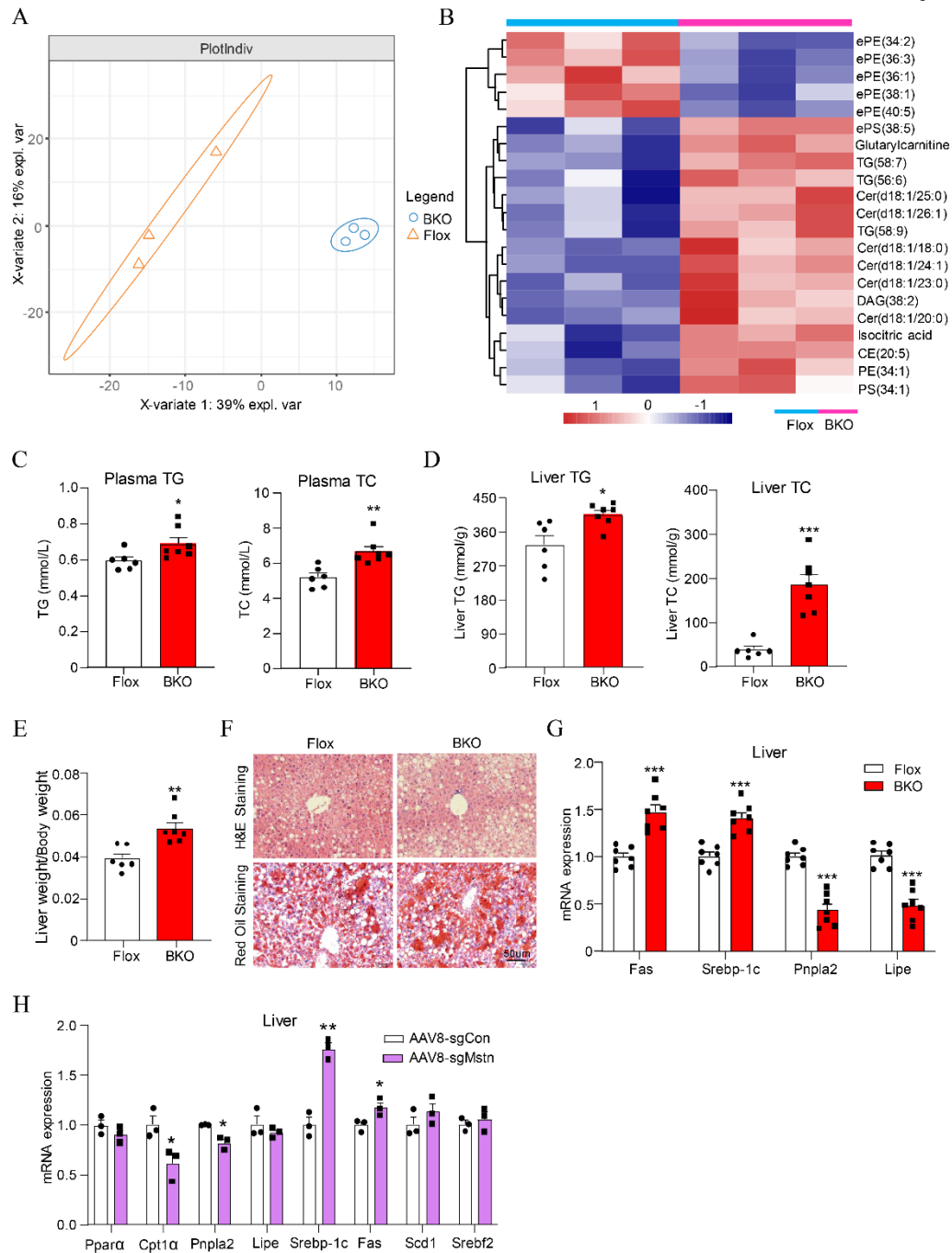


Figure 2. Myostatin ablation in BAT shows progressive fatty liver. **(A)** Principal component analysis plot of metabolomics from BKO and Flox groups. **(B)** The heatmap of the metabolites that significantly ($p < 0.05$) differences in BKO group versus control group. **(C)** Plasma TG and TC levels in BKO and Flox mice on 12-week HFD ($n = 6-7$). **(D)** Liver TG and TC levels in BKO and Flox mice on 12-week HFD ($n = 6-7$). **(E)** The ratio of liver of BKO and Flox mice on 12-week HFD ($n = 6-7$). **(F)** H&E and Oil red O staining of liver in BKO and

1 Flox mice on 12-week HFD (scale bars, 50 μ m). **(G)** Relative mRNA expression
2 of lipid metabolism related genes in liver of BKO and Flox mice on 12-week
3 HFD (n= 7). **(H)** Relative mRNA expression of lipid metabolism related genes
4 in liver of AAV8-sgCon and AAV8-sgMstn mice on 12-week HFD (n=3). All
5 results were shown as mean \pm SEM. * p <0.05, ** p <0.01, *** p <0.001. A two-tailed
6 Student t test was used for statistical analysis.

7

8

9

10

11

12

13

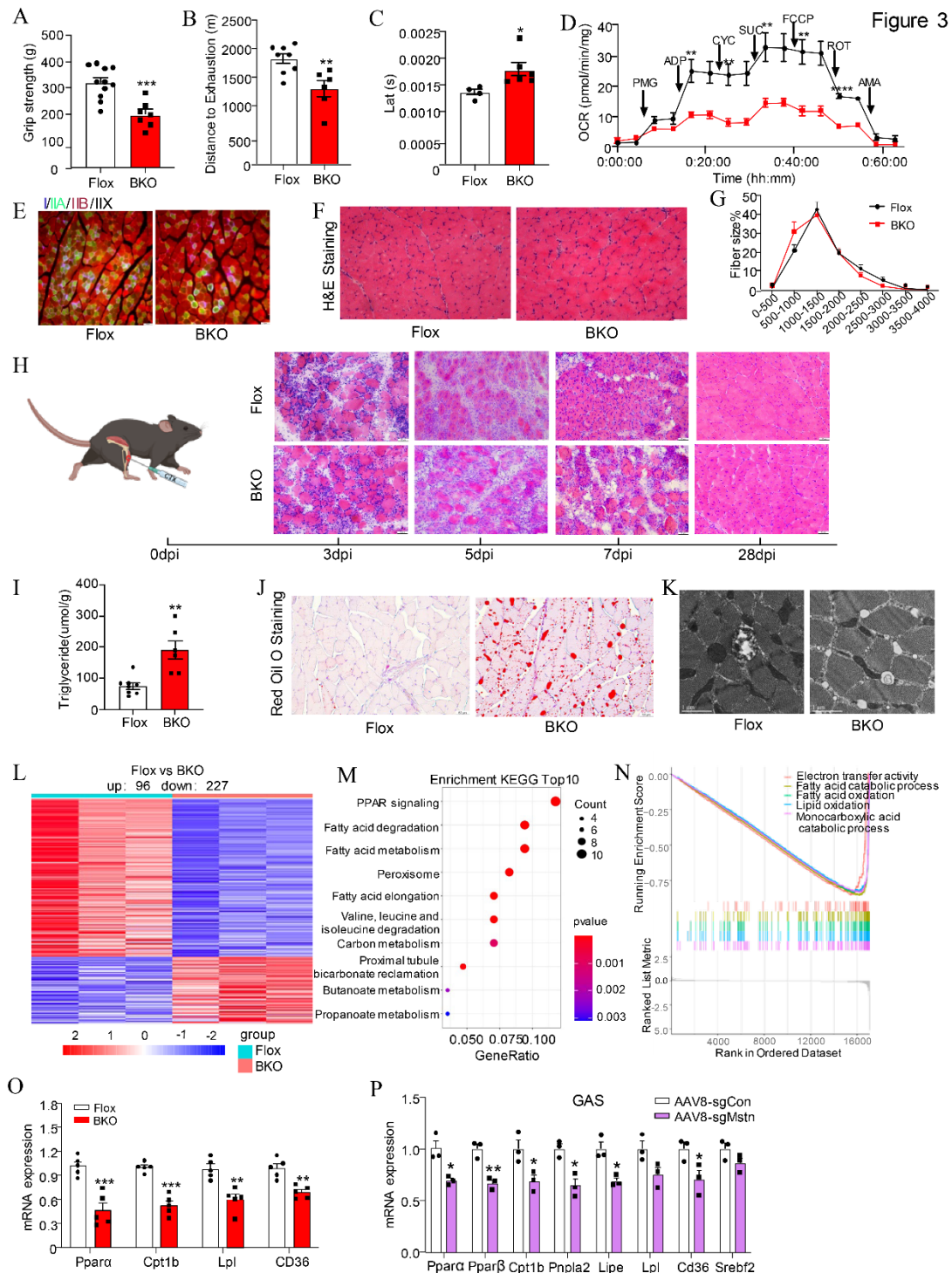


Figure 3. Myostatin ablation in BAT impairs the function of skeletal muscle. **(A)** Grip strength of male Flox and BKO mice on HFD (n= 7-11). **(B)** Total distance of male Flox and BKO mice on HFD in exhaustion test (n= 6-8). **(C)** Latency of compound muscle action potentials from the GAS of mice (n= 4-6). **(D)** OCR in GAS from BKO and Flox mice on HFD (n= 6). **(E)** Immunofluorescence analysis of fiber type composition in GAS. The different myosin heavy chain isoforms were stained in blue (MyHC-I), green (MyHC-IIa)

1 or red (MyHC-IIb) (scale bar, 50 μ m). **(F)** Representative H&E staining of GAS
2 from BKO and Flox mice on HFD (scale bar, 50 μ m). **(G)** Fiber cross-sectional
3 area (CSA) distribution and median CSA of GAS. **(H)** Representative H&E
4 staining of Tibialis Anterior, 3 days, 5 days, 7 days or 28 days after cardiotoxin
5 injury. **(I)** GAS TG level in BKO and Flox mice on 12-week HFD (n= 6-8). **(J)**
6 Representative Oil Red O staining of GAS from BKO and Flox mice on HFD
7 (scale bar, 50 μ m). **(K)** Representative electron micrographs of lipid droplets in
8 muscle of male mice (scale bars, 2 μ m). **(L)** Heatmap of 323 differential genes
9 of GAS from BKO and Flox mice on HFD. **(M, N)** KEGG and GSEA enrichment
10 analysis based on downregulated genes. **(O)** Relative mRNA expression of lipid
11 metabolism related genes in GAS of BKO and Flox mice on 12-week HFD (n=
12 5). **(P)** Relative mRNA expression of lipid metabolism related genes in GAS of
13 AAV8-sgCon and AAV8-sgMstn mice on 12-week HFD (n=3). All results were
14 shown as mean \pm SEM. * p <0.05, ** p <0.01, *** p <0.001. A two-tailed Student's t
15 test was used for statistical analysis.

16

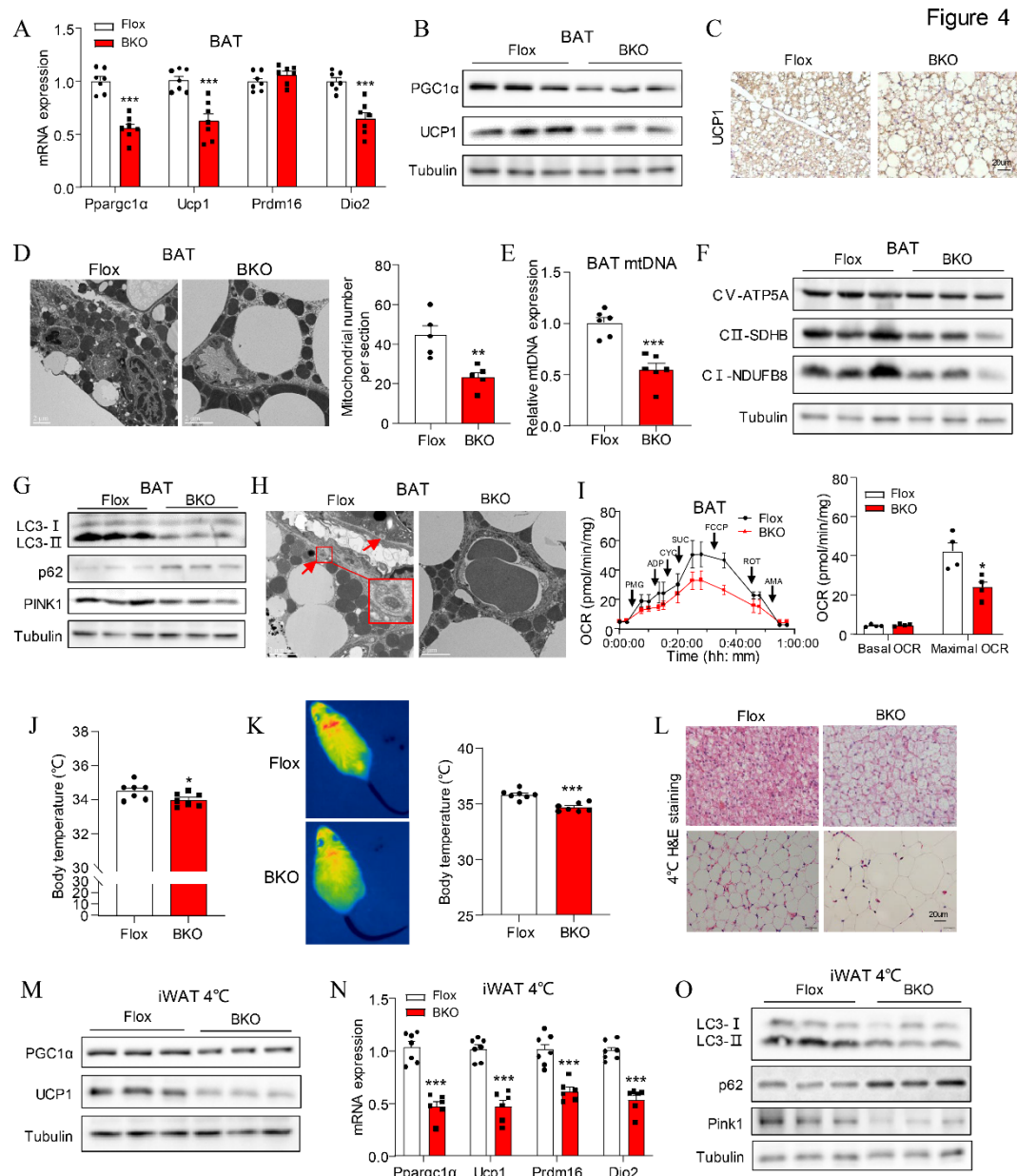


Figure 4. Loss of Myostatin attenuates mitochondrial biogenesis and mitophagy in BAT. **(A)** Relative mRNA expression of thermogenesis related genes in BAT of BKO and Flox mice on 12-week HFD (n= 7). **(B)** Western blot analysis of PGC1-α and UCP1 in BAT (n= 3). **(C)** UCP1 staining of BAT from BKO and Flox mice fed with 12-week HFD (scale bars, 20 μm). **(D)** Electron microscopy analysis of mitochondrial number in BAT. **(E)** Relative mtDNA number in BAT (n= 6). **(F, G)** Western blot analysis of mitochondrial complex

1 and mitophagy proteins (n= 3). **(H)** Electron microscopy analysis of mitophagy.
2 **(I)** OCR of the BAT. The basal and maximal OCR of mitochondrial complex II
3 (n= 4). **(J)** The body temperature of BKO and Flox mice after 7-days cold
4 exposure (n= 7). **(K)** Thermography assessment of the surface temperature of
5 indicated mice after 7-days cold exposure (n= 7). **(L)** H&E staining of BAT, iWAT
6 of BKO and Flox mice after 7-days cold exposure (scale bars, 20µm). **(M)**
7 Western blot analysis of PGC1-α and UCP1 in iWAT from BKO and Flox mice
8 after 7-days cold exposure (n= 3). **(N)** Relative mRNA expression of
9 thermogenesis related genes in iWAT from mice after 7-days cold exposure (n=
10 7). **(O)** Western blot analysis of mitophagy proteins in iWAT from BKO and Flox
11 mice after 7-days cold exposure (n= 3). All results were shown as mean ± SEM.
12 * $p < 0.05$, ** $p < 0.01$, *** $p < 0.001$. A two-tailed Student *t* test was used for statistical
13 analysis.

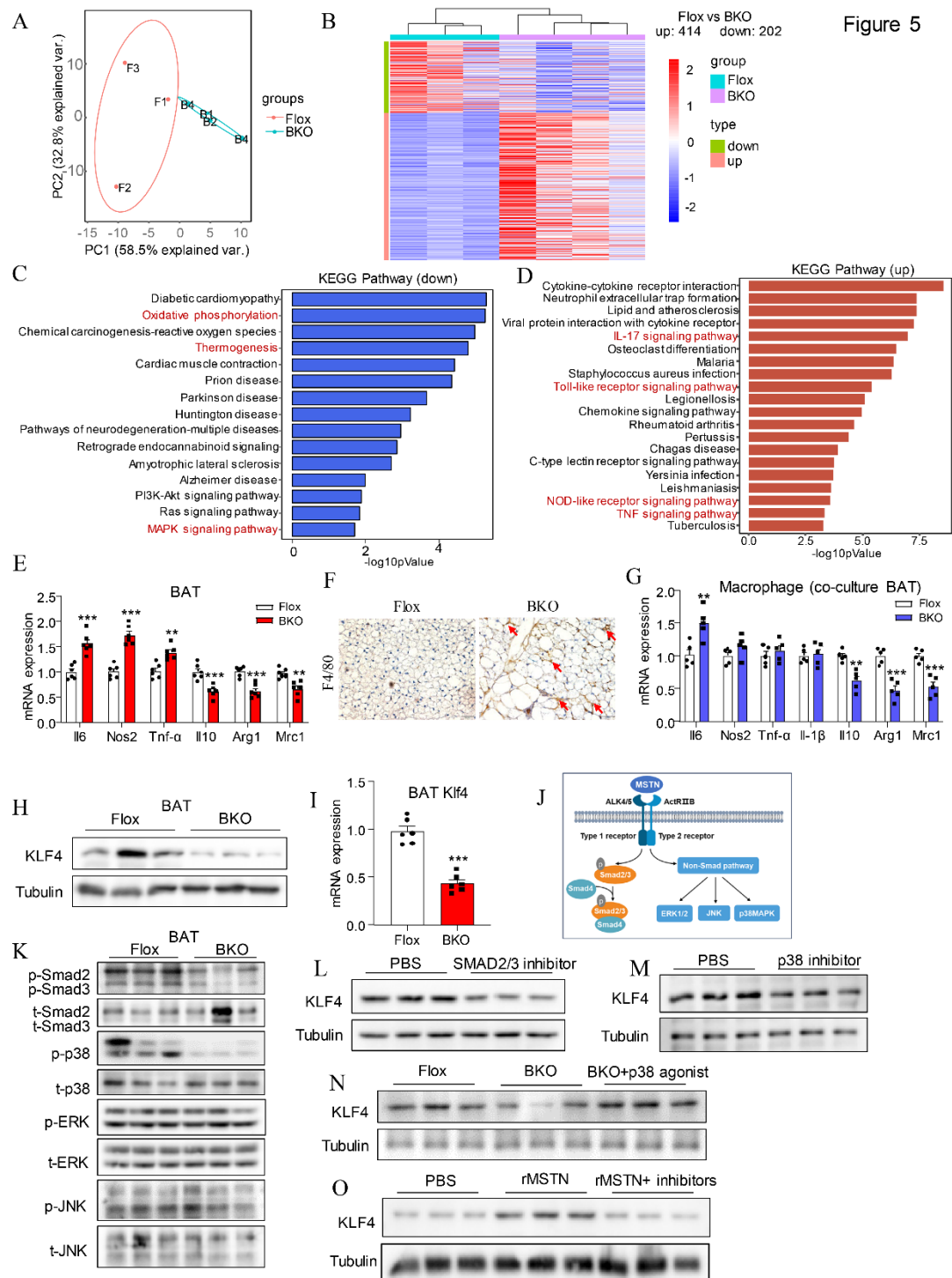


Figure 5. Myostatin ablation in BAT shows signatures of mitochondrial dysfunction and inflammation. **(A)** Principal component analysis plot of the BAT samples from the BKO and Flox groups. **(B)** Heatmap plot comparing 414 upregulation genes and 202 downregulation genes between BKO and Flox groups. **(C)** Enriched KEGG pathways for downregulation genes. **(D)** Enriched KEGG pathways for upregulation genes. **(E)** Relative mRNA expression of inflammatory genes (n= 6). **(F)** F4/80 staining of BAT (scale bars, 20 μm). **(G)** Relative mRNA expression of inflammatory genes in macrophages co-cultured

1 with BAT from BKO or Flox mice (n= 5). **(H)** Western blot analysis of KLF4 in
2 BAT (n=3). **(I)** Relative mRNA expression of Klf4 in BAT (n= 6). **(J)** Schematic
3 model of the downstream pathway of MSTN. **(K)** Western blot analysis of
4 Smad2/3 and non-Smad pathway in BAT from the BKO and Flox mice (n= 3).
5 **(L, M)** Western blot analysis of KLF4 in primary brown adipocytes treated with
6 PBS and SMAD2/3 inhibitor, or p38 inhibitor (n= 3). **(N)** Western blot analysis
7 of KLF4 in primary brown adipocytes from Flox or BKO mice. In BKO+p38
8 agonist group, primary brown adipocytes were treated with 1 μ M
9 dehydrocorydaline (n= 3). **(O)** Western blot analysis of KLF4 in primary brown
10 adipocytes treated with PBS, rMSTN, rMSTN+inhibitors, in rMSTN+inhibitors
11 group, primary brown adipocytes were treated with SMAD2/3 and p38 inhibitor
12 (n= 3). All results were shown as mean \pm SEM. ** p <0.01, *** p <0.001. A two-tailed
13 Student t test was used for statistical analysis.
14

Figure 6

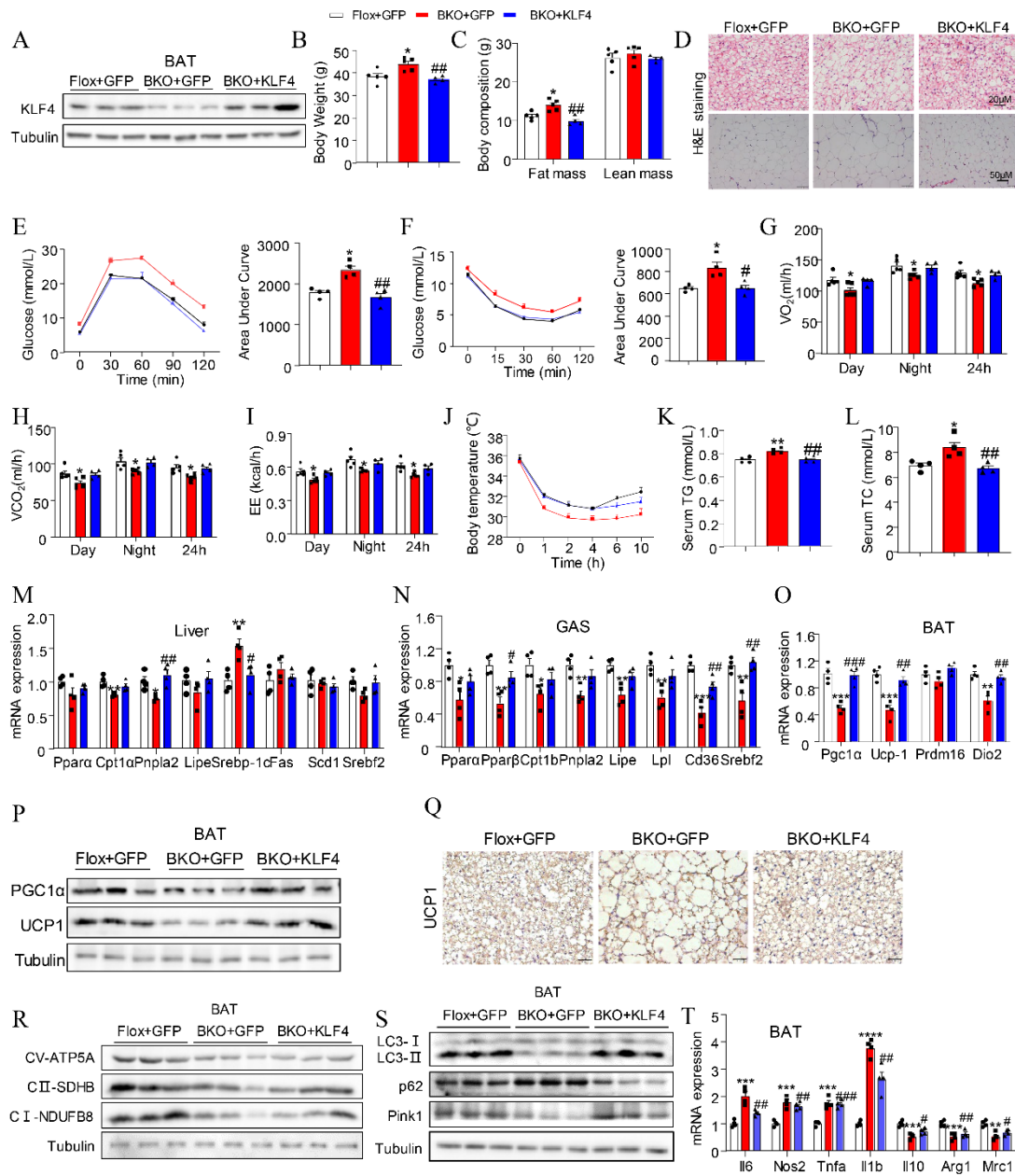


Figure 6. KLF4 is responsible for the metabolic phenotypes induced by Myostatin ablation. **(A)** Western blot analysis of KLF4 in BAT (n = 3). **(B, C)** The body weight, fat mass and lean mass of male Flox+GFP, BKO+GFP, and BKO+KLF4 mice on 12-week HFD (n = 4-5). **(D)** H&E staining of BAT, iWAT of male Flox+GFP, BKO+GFP, and BKO+KLF4 mice on 12-week HFD (BAT, scale bars, 20µm; iWAT, scale bars, 50 µm). **(E, F)** The glucose tolerance test (GTT) and insulin tolerance test (ITT) in male Flox+GFP, BKO+GFP, and BKO+KLF4 mice on 12-week HFD (n = 4). **(G-I)** The oxygen consumption, carbon dioxide

1 production, and energy expenditure of male Flox+GFP, BKO+GFP, and
2 BKO+KLF4 mice on 12-week HFD (n= 4-5). **(J)** The body temperature of male
3 Flox+GFP, BKO+GFP, and BKO+KLF4 mice during cold challenges (n= 4). **(K,**
4 **L)** Plasma TG and TC levels (n= 4). **(M, N)** Relative mRNA expression of lipid
5 metabolism related genes in the liver or GAS (n= 4). **(O)** Relative mRNA
6 expression of thermogenesis related genes in BAT (n= 4). **(P)** Western blot
7 analysis of PGC1- α and UCP1 in BAT (n= 3). **(Q)** UCP1 staining of BAT (scale
8 bars, 20 μ m). **(R, S)** Western blot analysis of mitochondrial complex and
9 mitophagy proteins in BAT (n= 3). **(T)** Relative mRNA expression of
10 inflammatory genes in BAT (n= 4). All results were shown as mean \pm SEM.
11 * p <0.05, ** p <0.01, *** p <0.001, compared with the Flox+GFP group; # p <0.05,
12 ## p <0.01, ### p <0.001, compared with the BKO+GFP group. A one-way ANOVA
13 followed by Bonferroni post-tests was used for three groups statistical analysis.
14

Figure 7

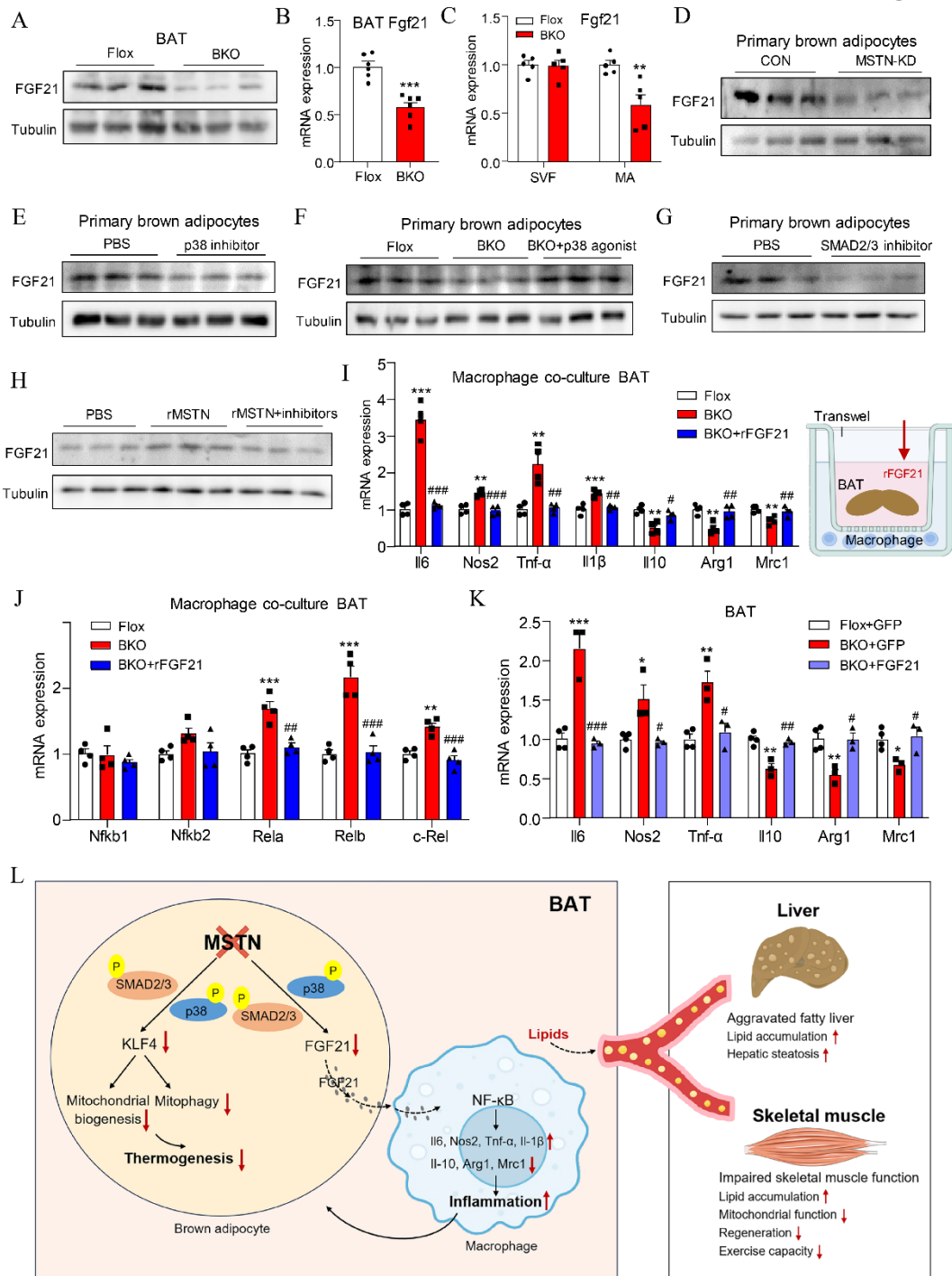


Figure 7. FGF21 contributes to the inflammatory phenotypes induced by Myostatin ablation. **(A)** Western blot analysis of FGF21 in BAT from BKO and Flox mice on 12-week HFD (n= 3). **(B)** Relative mRNA expression of Fgf21 in BAT (n= 6). **(C)** Relative mRNA expression of Fgf21 in BAT SVF and mature adipocytes from BKO and Flox mice on 12-week HFD (n= 5). **(D)** Western blot analysis of FGF21 in primary brown adipocytes of control and MSTN-knockdown groups (n= 3). **(E)** Western blot analysis of FGF21 in primary brown adipocytes treated with PBS or p38 inhibitor (n= 3). **(F)** Western blot analysis

1 of FGF21 in primary brown adipocytes from Flox or BKO mice. In BKO+p38
2 agonist group, primary brown adipocytes were treated with 1 μ M
3 dehydrocorydaline (n= 3). **(G)** Western blot analysis of FGF21 in primary brown
4 adipocytes treated with SMAD2/3 inhibitor (n= 3). **(H)** Western blot analysis of
5 FGF21 in primary brown adipocytes treated with PBS, rMSTN, rMSTN+
6 inhibitors (n= 3), in rMSTN+inhibitors group, primary brown adipocytes were
7 treated with SMAD2/3 and p38 inhibitor. **(I, J)** Relative mRNA expression of
8 inflammatory genes **(I)** and NF- κ B signaling pathway related genes **(J)** in
9 macrophages co-culture with BAT from Flox and BKO mice. In BKO+rFGF21
10 group, macrophages were additionally treated with 100 nM rFGF21 (n= 4). **(K)**
11 Relative mRNA expression of inflammatory genes in BAT from Flox, BKO+GFP
12 or BKO+FGF21 mice (n= 3-4). **(L)** Working model. All results were shown as
13 mean \pm SEM. ** p <0.01, *** p <0.001, compared with the Flox group; # p <0.05,
14 ## p <0.01, ### p <0.001, compared with the BKO group. A two-tailed Student t test
15 was used for two groups statistical analysis. A one-way ANOVA followed by
16 Bonferroni post-tests was used for three groups statistical analysis.